ORIGINAL ARTICLE

Development and use of semi-empirical spectral ground motion models for GPP-induced micro-earthquakes in Southern Germany

Francesca Taddei[1] · Sabrina Keil[2] · Ali Khansefid[3] · Aditi Kumawat[1] · Felix Schneider[1] · Johachim Wassermann[2] · Gerhard Müller[1]

Abstract

This study provides a comprehensive exploration of ground motions associated with micro-earthquakes induced by geothermal power plants (GPP) in Southern Germany and proposes corresponding ground motion prediction equations (GMPE). Initiating with a statistical analysis of recorded seismic data from the GPP in Insheim, the study is extended to the greater Munich area. For the latter, the scarce recorded data are merged with physics-based simulation data. The recorded data in Insheim, Poing, Unterhaching and the simulated data in Munich are compared to existing GMPEs for GPP-induced events, highlighting the need of new region-specific prediction equations. The proposed GMPEs are expressed in terms of peak quantities, spectral accelerations and velocities, separating the horizontal and vertical direction. The regression curves exhibit a good alignment with both recorded and simulated data, within an acceptable range. Notably, the results reveal higher spectral quantities at shorter periods (< 0.1 s), underscoring the importance of this characteristic in seismic assessment. The article shows an exemplary application for a low-rise residential building, located at a hypocentral distance of 3 km. While the building meets serviceability standards for an M_W up to 2.5, the verification fails at $M_W = 3$, emphasizing the need for robust risk assessment. These findings contribute to the understanding of ground motions of GPP-induced events, offering practical implications for serviceability verifications and aiding informed decision-making in geothermal energy projects.
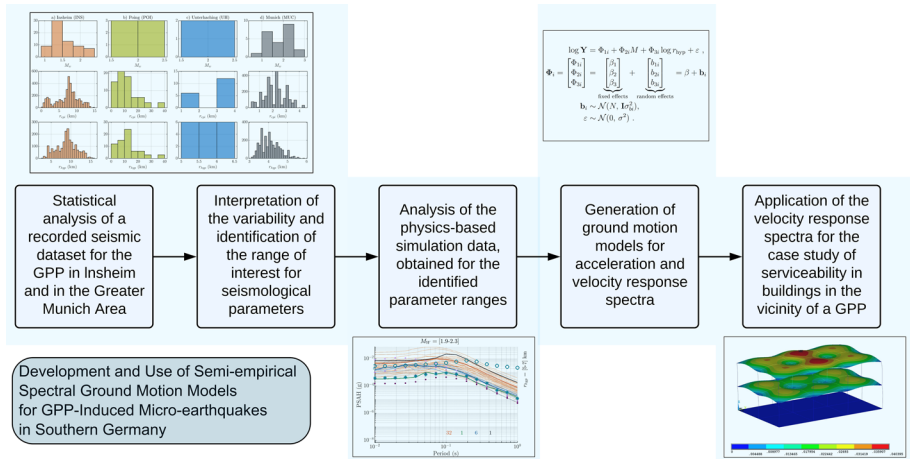
Extended author information available on the last page of the article

Graphical abstract

1 Introduction

1.1 GPP-induced micro-earthquakes in Southern Germany

Geothermal energy is rapidly gaining prominence in Germany's renewable energy landscape. Bavaria stands as the top of deep geothermal utilization in Germany, boasting approximately 90% of the country's installed capacity in this sector. The region has become a hotspot for harnessing geothermal energy, particularly for heating purposes. There are also geothermal power plants (GPP) in the planning stages, such as Michaelibad and Pullach Süd, indicating a continued commitment to the growth of geothermal energy in the region.

Geothermal energy provides a clean and renewable power source but is associated with induced seismicity risks in certain regions, requiring careful monitoring and mitigation measures. In hydro-geothermal power plants, the re-injection of cold water (with a spread temperature of approx. 60 °C or higher) even under only small to moderate over-pressure conditions can lead to a re-orientation and modification of the in-situ stress conditions on existing nearby faults which may in turn fail by triggering mostly small slips of the corresponding fault (BGR 2023). These micro-earthquakes are usually addressed to as triggered, and the related moment magnitudes range from 1 to 3. In hot dry rock (HDR) and enhanced geothermal systems (EGS), the initiation of new cracking processes is essential for operation and the micro-events are addressed to as induced. The induced earthquakes in these systems can sometimes reach larger magnitudes compared to those observed in hydro-geothermal power plants. The focal depth of GPP-induced and GPP-triggered earthquakes varies between 1 and 10 kms, depending on local geophysical conditions and the depth of injection wells. Furthermore, the epicenters of these micro-earthquakes are

usually situated very close to GPP stations, frequently within a 10-km radius (Khansefid et al. 2022). In contrast to moderate and large earthquakes, which tend to rupture a significant portion of the seismogenic layer, small earthquakes like those induced and triggered by geothermal systems are typically characterized by ruptures spanning less than a kilometer. Consequently, the rupture depth will significantly influence the velocity map of the soil surface (Douglas et al. 2013).

Given their proximity to urban areas, GPPs are often situated near communities, making the microseismic activity perceptible even when the magnitudes are low (Grünthal 2014). It is imperative to comprehensively investigate the uncertainties associated with this process and address public concerns regarding induced seismicity at GPP sites. An extensive review of worldwide case histories regarding felt induced seismicity in geothermal systems, along with a summary of the key mechanisms responsible for inducing seismicity, can be found in Buijze et al. (2019).

In Germany, GPPs located in cities such as Landau, Insheim, and Unterhaching have stirred substantial attention and concern within local communities over the past decade. However, it's essential to note that, when compared to other forms of seismic activity, the risk associated with GPP-induced seismicity is relatively low. A comprehensive study on induced seismicity in Central Europe revealed that the maximum observed magnitude of induced seismicity at geothermal sites is the smallest among potential types of induced or triggered seismic events and significantly lower than the maximum observed or expected magnitudes of natural tectonic earthquakes at the sites under investigation (Grünthal 2014). Southern Germany represents an exception: in a recent study about the Upper Rhine Graben (Insheim and Landau geothermal fields) and Bavarian Molasse (Unterhaching geothermal field), it was found that the contribution of induced seismicity to the total seismic hazard is higher than that of natural seismicity in both areas (Sisi et al. 2017). This is due to the very low tectonic activity in the considered regions and it applies only for small events with short return periods (Schlittenhardt et al. 2014).

Southern Germany is a hotspot for harnessing geothermal energy, with a clear commitment to further growth in this sector. As the geothermal power plant industry expands, it is crucial to estimate the seismic risk, even if small, to reassure the public. However, there is a lack of site-specific prediction models for ground motions and building spectral motions, which are essential tools for an accurate risk assessment. Therefore, this study presents the development and application of new ground motion models for micro-earthquakes triggered by geothermal power plants in Southern Germany. Although this contribution exclusively focuses on hydro-geothermal power plants and the corresponding triggered seismic events, in the following, we utilize the adjective 'geothermal-induced (GI)' to denote the micro-earthquakes under consideration.

1.2 Ground motion prediction equations and logic-tree analysis

Seismic hazard and risk analysis, whether in highly active or tectonically stable regions, encounters challenges due to limited shaking observations, especially for small to moderate earthquakes. Traditional purely empirical ground motion models (GMMs) may lack constraints within these regions. A prevailing approach in engineering practice involves adapting GMMs originally designed for active areas to the specific seismological conditions of the target region. This adaptation incorporates simulations calibrated to source, path, and site properties derived from weak motion recordings within the target area or alternative data sources. To address epistemic uncertainty within the ground

motion model, rather than employing existing multiple independent models, a novel concept involves utilizing a core model (the backbone) and applying scaling factors to account for uncertainties in the seismological properties of the target region (Weatherill and Cotton 2020; Boore et al. 2022).

To facilitate the application of the backbone approach in large-scale seismic hazard assessments at national and continental levels, a straightforward ground-motion logic tree has been proposed (Grünthal 2014). This logic tree aims to address potential variations in average stress drop, inelastic attenuation, and the inherent statistical uncertainty in regression-based models across different regions. It assumes that regions with limited historical data will exhibit variations in ground motion characteristics similar to regions with extensive strong-motion databases. However, this approach may have limitations, particularly in tectonically stable areas, where the range of ground motion predictions could be too narrow.

A subset of GMMs are the ground motion prediction equations (GMPE), mathematical expressions used to quickly estimate the expected intensity measure, such as peak ground acceleration (PGA), peak ground velocity (PGV), or spectral accelerations (SA), at a particular location resulting from an earthquake at a specific distance and magnitude. Empirical GMPEs are derived from statistical analyses of observed ground motions from past earthquakes. Semi-empirical GMPEs incorporate both empirical relationships and physical principles. Physics-based GMPEs rely on fundamental earthquake physics and simulate ground motions through numerical simulations of the seismic wave propagation. The choice of GMPE depends on the available data and the specific needs of a seismic hazard assessment (Atkinson 2015).

GMPEs take various parameters into account to estimate ground motion characteristics resulting from an earthquake. These parameters typically encompass essential factors such as magnitude M (moment magnitude scale M_W and/or local magnitude M_L), distance to the site of interest, site conditions (V_{s30}), focal depth (D) and rupture mechanism, among other potentially relevant variables.

The recorded or simulated data can undergo elaborations using analysis of variance (ANOVA) and/or regression methods. These two types of empirical data analysis, ANOVA and regression, complement each other. In ANOVA, no specific functional form of the mentioned parameters is presupposed, but it necessitates a substantial dataset with multiple records from overlapping magnitude-distance ranges across various locations. Conversely, in regression analysis, a functional form must be employed, but it does not require data from different parameter ranges to overlap, making it suitable for sparse data sets.

Induced earthquakes are expected to have smaller magnitudes and shallower depths compared to the tectonic earthquakes used in most GMPEs. While GMPEs for larger earthquakes are designed for a broader use across various locations, the unique attributes of induced earthquakes call for tailored models suited to specific applications due to their distinct characteristics. For example, for induced micro-earthquakes in Southern Germany relevant risk scenarios are characterized by magnitudes between 1 and 3 and shallow depths between 2 and 6 km. Moreover, the significant distance from the epicenter ranges from 2 to 5 km.

In the GMPEs, the soil conditions are usually given in terms of specific V_{s30} or standard soil classes. To standardize all recorded accelerograms to a uniform soil condition requires the intricate task of mitigating the inherent amplification effects at the site. However, effectively removing these amplification effects remains a challenge.

For very-near-sources ($r_{epi} < 7\ km$), the PGV varies significantly at different locations and does not follow typical attenuation behaviors assumed for larger distances (Ntritsos

et al. 2021). The challenges associated with developing equations for estimating ground motions from induced earthquakes are discussed in Bommer et al. (2016) and can be summarized as follows:

- Compared to tectonic earthquakes, induced earthquakes are characterized by a larger spatial variability and regional variations in ground motion characteristics, particularly at smaller magnitudes (Douglas 2004).
- Generally, existing empirical GMPEs do not extrapolate reliably to smaller magnitudes (Atkinson and Assatourians 2017).
- Due to the shallow focal depths of induced earthquakes, typically confined to the upper 5 km of the Earth's crust, the heterogeneous properties of the upper crust influences significantly the wave propagation pattern (Ntritsos et al. 2021).

On the other hand, other aspects facilitate the development of targeted GMPEs:

- The uppermost crustal arrangement and the soil condition are well known, especially from the boring process.
- Single seismic source and propagation along a narrow range of travel paths allow nonergodic standard deviations to be used. This can offer insights into single-station, single-source variability (Atkinson 2006; Rodriguez-Marek et al. 2011).
- A greater number of induced events compared to natural seismic events is observed. Because GPP need to be instrumented by law, there is a chance to regularly enhance and refine GMPEs, thereby decreasing inherent uncertainties related to the specific application.

1.3 Existing GMPE models

Table 1 shows existing GMPEs models for different induced seismicities in Europe and worldwide, along with the considered ranges of moment magnitude and distances. Some of these models are further discussed, to explain the choice of the model in the present study.

Among the most extensive studies on GMPEs for induced earthquakes, the study in Douglas et al. (2013) proposed a set of 36 models derived from stochastic models. The study covers ranges of magnitudes, distances and seismological parameters similar to the ones observed for Southern Germany. The study also shows a ranking and weighting approach of the proposed GMPE for an application for the Campi Flegrei in Italy, where the magnitudes of the available data cover the range of $0.4 \leq M_W \leq 2.1$. From the 36 models one can select the most appropriate subset and assign weights depending on the fit to the data. The study shows the importance of including several models in the logic tree due to the high level of epistemic uncertainty inherent in seismic hazard assessments with limited observations.

Another approach is proposed in Atkinson (2015), where the author analyzed tectonic seismic events with magnitudes between 3 and 6, occurring at distances less than 40 km from the epicenter, sourced from the Next Generation Attenuation-West 2 (NGA-West 2) database. The developed GMPE aligns well with the NGA-West 2 database and a stochastic point-source simulation model. However, due to data sparsity at close distances, there is potential uncertainty, possibly up to a factor of 2, in ground-motion amplitudes within 10 km of the hypocenter. A crucial finding suggests that ground-motion amplitudes for moderate induced events may be significantly larger near the epicenter than

Table 1 Recent GMPE for different induced seismicities in Europe and worldwide

Human activity, M, r_{hyp} in km	Location	References	GM-parameter
Hydraulic fracture $M = [0,3]$ $r_{hyp} = [0,10]$	UK (Preston New Road shale gas site)	Cremen et al. (2020)	PGA, PGV, PSA
Gas extraction $M = [1.8,3.6]$ $r_{hyp} = [3,30]$	Netherlands (Groningen gas field)	Dost et al. (2017) and Bommer et al. (2022)	PGV
Gas extraction $M = [2.5,7.25]$ $r_{hyp} = [3,60]$	Netherlands (Groningen gas field)	Dost et al. (2017) and Bommer et al. (2022)	PGA, PSA
GPP $M = [1.3,3.3]$ $r_{hyp} = [0,20]$	California (Geysers)	Prezioso et al. (2022)	PGA, PGV, PSA
GPP $M = [2.5,5.5]$ $r_{hyp} = [0,100]$	Worldwide	Khansefid et al. (2023)	PGA, PGV, PSA
GPP $M = [3.5,4.9]$ $r_{hyp} = [0,200]$	Italy (Campi Flegrei)	Douglas et al. (2013)	PGA, PGV, PSA
Fluid injection $M = [3.5,5.8]$ $r_{hyp} = [2,500]$	US (Oklahoma)	Novakovic et al. (2018)	PGA, PSA
Fluid injection $M = [3.0,5.8]$ $r_{hyp} = [0,500]$	US (Texas, Oklahoma, and Kansas)	Zalachoris and Rathje (2019)	PGA, PGV, PSA
EGS $M = [1.9,3.1]$ $r_{hyp} = [2,8]$	Australia (Cooper Basin)	Edwards and Douglas (2013)	PSA

predicted by most NGA-West 2 GMPEs. This heightened motion potential is attributed to the shallow depth of induced events, placing the earthquake fault very close to the epicenter.

A more recent study involved the analysis of a worldwide database of 110 GPP-induced earthquakes with 664 recorded accelerograms, calculating their seismic characteristics, and developing various ground motion models to simulate peak values, duration, spectral acceleration, and velocity in both horizontal and vertical directions (Khansefid et al. 2023). The outcome of this study was further employed to relate the seismic characteristics with the operational parameters, such as the power plant injection rate (Khansefid et al. 2022). The corresponding hazard model can be used by engineers and scientists for risk assessment and risk mitigation through safe operation plans of the GPPs.

Site-specific GMPEs for Unterhaching, Landau and Insheim are proposed in Sisi et al. (2017), where existing models for tectonic earthquakes are weighted based on a four-step process. The focus of the study was on Gutenberg–Richter law (GR law), which relates a certain magnitude M_i (and/or the PGV) and the frequency of occurrence of earthquakes with magnitude > M_i. However, no details are given for spectral acceleration and velocity.

By employing recorded data pertaining to the Insheim geothermal reservoir in Germany, a further study (Taddei et al. 2022) delved into the key seismological attributes. It conducts a statistical assessment of the spectral characteristics relative to the magnitude and the site-to-source distance, while also generating elastic response spectra for the chosen GI-events and monitoring stations. The study also showed the importance of the spectral characterization of the ground motion. It deduced that the vertical and horizontal components of the motion exhibit distinct frequency characteristics, requiring separate treatments. Frequencies above 15 Hz predominantly influence the vertical component's response, whereas frequencies below 10 Hz impact the horizontal component, with a notable difference in magnitude.

Ground motion estimations can be carried out with physics-based deterministic approaches. In regions characterized by low tectonic seismic activity, such as Germany, obtaining accurate local GMPEs can be challenging. To address this, in Steinberg et al. (2023) the authors introduced an innovative approach to generate comprehensive ground motion maps using full seismic waveforms for different sources and machine learning.

Further studies assessed the impact of uncertainties encompassing event parameters and the subsurface model on the calibration of PGV values in horizontal direction, using 3D seismic simulations (Keil et al. 2022). The simulations exhibit overall agreement with the recorded ground motion waveform. In the same study, the shake maps for different events showed that the area with the largest ground motion occurs around 2.5 km south of the epicenter. This was confirmed by the felt intensity reports transmitted by the population after the considered events (Groos et al. 2013).

1.4 Scope of this study

In this contribution, we explore the ground motions for GPP-induced micro-earthquakes in Southern Germany. Figure 1 shows the overview of the tasks performed in this study. We initiate with a statistical analysis of a recorded seismic dataset for the GPP in Insheim and the broader Munich region. We then merge the scarce dataset from Munich with physics-based simulation data, and generate ground motion models expressed in terms of response spectra. Lastly, we illustrate the practical utility of the developed response spectra through an exemplary application for serviceability issues.
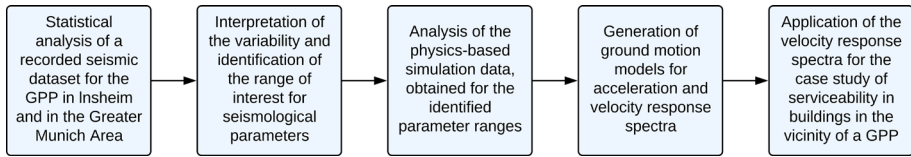
Fig. 1 Overview of the tasks performed in this study

2 Geothermal areas and GPPs

Table 2 provides essential information about the considered geothermal power plants.

The Upper Rhine Graben (URG) is a highly exploited region for geothermal energy production in Germany, primarily due to its elevated geothermal gradient, which reaches over 150 degrees Celsius at depths of 2500 ms in the northern URG. Figure 2 shows the map of deep geothermal projects in the URG (Dalmais et al. 2022). Despite the URG being one of Germany's most seismically active areas, the seismic risk remains relatively low to moderate when compared to the broader tectonic context of Europe. Since the start of operations at the Insheim and Landau geothermal reservoirs in the URG in 2006, more than 2200 induced microseismic events have been detected in the vicinity of these reservoirs. Some of these events in Insheim have registered a magnitude exceeding 2 (Vasterling et al. 2017). Considering the high number of induced microseismic events, the data set for Insheim in the magnitude range M_W between 0.5 and 2.2 is well-populated.

The Molasse basin (MB), located north of the Alps, spans approximately 700 km in an E-W direction and 130 km NS. It is filled with Tertiary sediments up to 5000 m thick, categorized into five groups by age. These sediments overlay Mesozoic limestone layers and the Variscan crystalline basement. Due to the southward dip of the limestone layers, the reservoir's depth and water temperature increase toward the Alps, with depths reaching 2.3–2.5 km and temperatures of 85 °C in the study area. The Poing geothermal project encompasses two wells, Th1 (injection well) and Th2 (production well), drilled to depths of 3050 and 3014 m TVD, respectively. The circulation commenced in December 2012, reaching maximum flow rates of 100 l/s. Notably, seismic activity was first recorded towards the end of 2016, with two larger events boasting local magnitudes of 2.1 and 1.8, along with several smaller aftershocks. Another event with a local magnitude of 2.1 occurred on September 9th, 2017 (Keil et al. 2022).

The Unterhaching geothermal power plant has an electrical capacity of around 3.36 megawatts and a thermal capacity of up to 70 MW (Wolfgramm et al. 2007). It began operations in 2007, utilizing the Kalina process for electricity generation, with seismicity starting in 2008. The Kalina plant was later decommissioned in 2017 due to shifting priorities toward district heating for more households. In 2013, an event was recorded, with two successive shocks with a local magnitude of 1.9. Figure 3 shows the map of deep geothermal projects in the Molasse basin (Beichel et al. 2014).

In the subsequent sections, the term *location* refers to the geothermal projects and not to individual recording stations. On the other hand, the term *region* denotes an area encompassing multiple nearby GPPs, with specific references such as INS for Insheim and G.MUC for the locations comprising Poing, Unterhaching, and Munich.
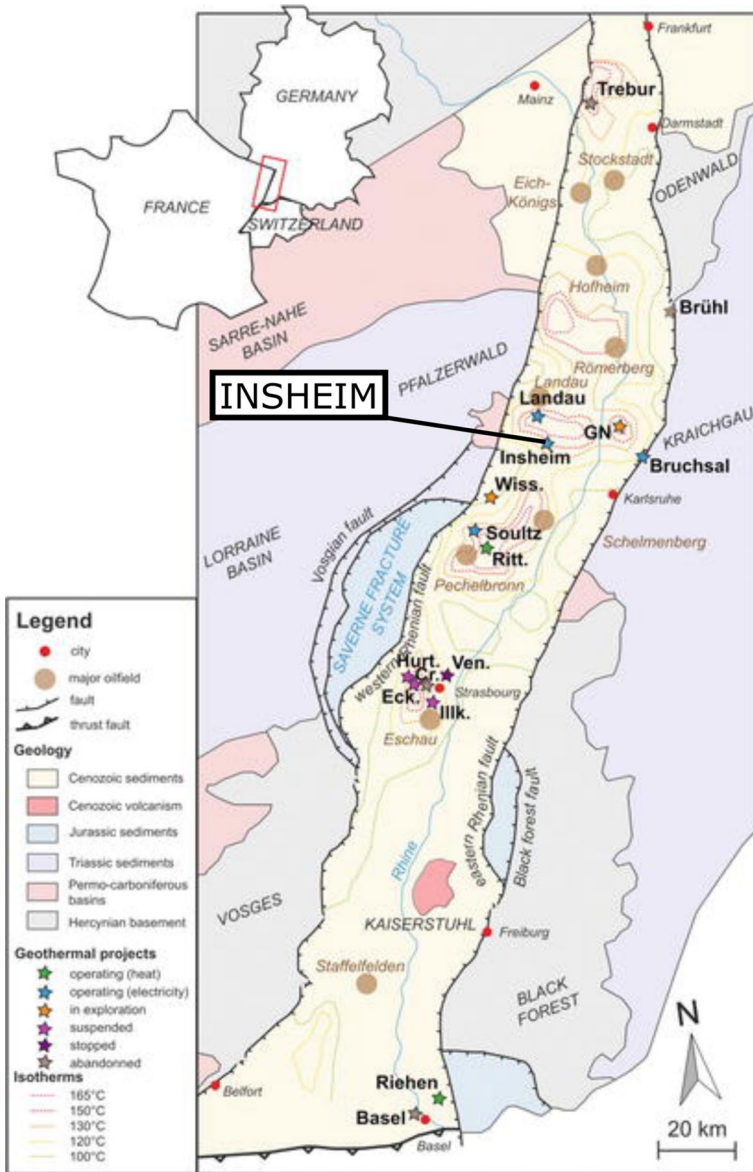
Fig. 2 Map of deep geothermal projects in the URG, highlighting the location of Insheim. The original image can be found in Dalmais et al. (2022)

3 Data

3.1 Data collection

GMPEs can be formulated through the examination of both recorded and simulated seismic ground motions. Utilizing ground motions captured from past earthquake
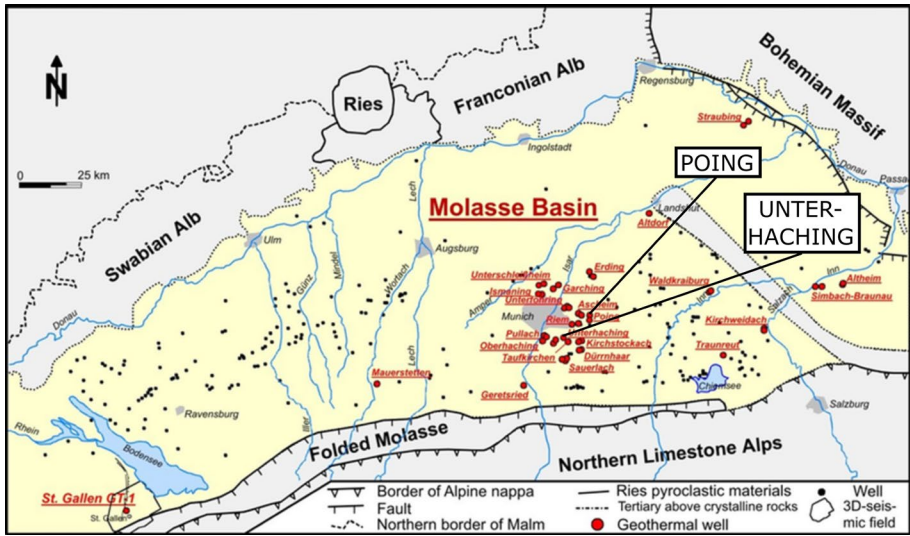
Fig. 3 Map of deep geothermal projects in the MB, highlighting the location of Poing and Unterhaching. The original image can be found in Beichel et al. (2014)

Table 2 Key data of the considered geothermal power plants

GPP	Start time	LAT (DMS)	LON (DMS)	Max. well depth (km)
Insheim	2007	49° 9' 0"	8° 9' 0"	3.8
Poing	2016	48° 11' 24"	11° 47' 24"	3.0
Unterhaching	2007	48° 3' 36"	11° 36' 0"	3.6

events provides indispensable data for calibration and validation purposes. Conversely, simulated ground motions offer valuable insights into potential seismic scenarios that may not have been observed in recorded data. In this study, we present recorded data for Poing (POI) and Unterhaching (UH) in the Greater Munich Area, comparing them with data from a third location outside Bavaria, Insheim (INS). Furthermore, we expand this comparative analysis by incorporating simulation data for a GPP in the city center of Munich (MUC), varying seismological parameters within a realistic range.

For Insheim, we used public data available from selected stations, retrieved from the ORFEUS database (Lanzano et al. 2021). A detailed description of the data retrieval is given in Taddei et al. (2022).

For Poing and Unterhaching, the raw data were provided by the Department of Earth and Environmental Sciences at LMU.

Most of the induced seismic events of this study are originally provided with their local magnitude M_L (Grünthal 2014). For the conversion from instrumentally measured M_L to M_W, we apply the following rules as proposed by Allmann et al. (2010) and described in Eq. 1, where the values between brackets give the standard deviation of the estimated M_W. This approach is based on recommendations from Schmitt and Günter (2015, 2014), which suggest using specific conversion relationships for
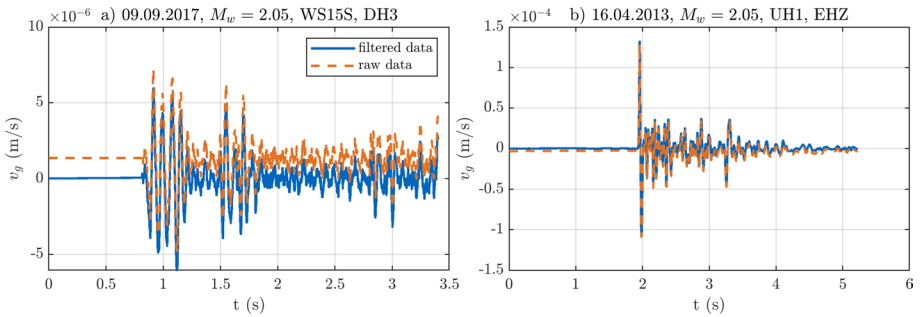
Fig. 4 Demonstration of waveform enhancement using baseline correction and bandpass filters. The details about the events, stations, and channels are given above each subplot

Germany. These recommendations are derived from a comparative analysis of various literature sources and a dedicated regression study.

$$
\begin{aligned}
M_L < 2 : \quad & M_W = 0.594 M_L + 0.985 \ (\pm 0.159) \\
2 \leq M_L < 4 : \quad & M_W = 1.327 + 0.253 M_L + 0.085 M_L^2 \ (\pm 0.134) \\
M_L \geq 4 : \quad & M_W = M_L - 0.3 \ (\pm 0.175)
\end{aligned}
\tag{1}
$$

It must be pointed out that scaling moment magnitudes from local magnitudes introduces additional uncertainties in the derivation of the GMPE, especially at low magnitudes (Edwards et al. 2010). In this study, we develop GMPEs for both M_W and M_L: the former serves as a benchmark for comparison with international models, while the latter is tailored for use in local projects and applications.

We ensured the raw data's integrity and correctness through a series of enhancements, including wavelet denoising, baseline adjustment, and high-pass filtering, as detailed in previous works (Khansefid et al. 2023, 2019). Figure 4 shows an example of waveform enhancement for two stations in the broader Munich area. This methodology has been effectively applied to enhance seismic recordings characterized by low amplitudes during GI-events and low-intensity signals in the Iranian plateau. Additionally, stations may feature multiple sensors with distinct characteristics, and these are distinguished using channel codes following the conventions described in Halbert (2023).

3.1.1 Recorded data for Insheim

The data of Insheim refer to two time periods: from October 2009 to July 2016 and from November 2020 to January 2023. In the first period, for the 17 chosen events, the moment magnitude values (M_W) ranged from a minimum of 1.5 to a maximum of 2.4, all occurring within a 2-kilometer radius of the Insheim GPP. Waveform data for 13 out of 17 events were accessible.

In the second period, more than 55 earthquakes were registered by the detector of the the MAGS (Microseismic Activity of Geothermal Systems) project (BGR 2023a). Two of them were of tectonic origin, one west of Eschbach (magnitude Ml = 1.6, depth 5 km), a second west of Neustadt an der Weinstraße (magnitude Ml = 0.5, depth 20 km). The other earthquakes could be assigned to the geothermal reservoirs of Landau and Insheim, respectively. All events remained below the human perception threshold (BGR 2023b).
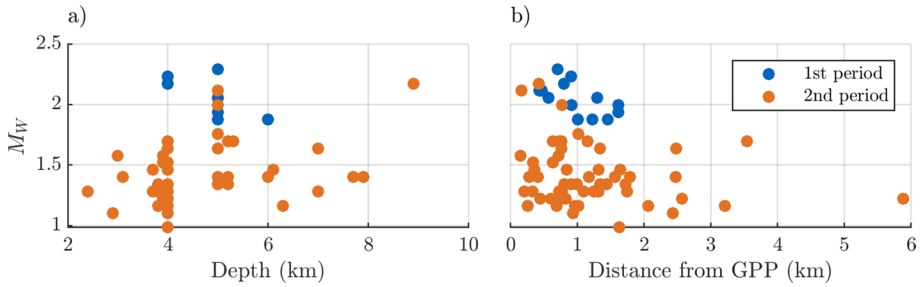
Fig. 5 INS: distribution of the magnitude of the selected events with respect to a) the event depth in km and b) the epicentral distance from the GPP in km

Figure 5 shows the distribution of the magnitude of the selected events with respect to the event depth and the epicentral distance from the GPP. Tabulated details of these events are provided in the annex, in Table 16, 17 and 18, with assigned numbers exclusively for those with available recordings. For the second period, the event-station matrix is available in form of a digital file in data and resources. The event times are consistently presented in local time. Additionally, Fig. 6 illustrates the geographic distribution of the selected events, along with their respective moment magnitudes (M_W) and depth in km. Figure 7 shows the selected stations for Insheim along with the location of the considered GPP. For Insheim, the surface lies at −0.25 km with respect to the mean sea level. The V_s in the range of depth between −0.25 km and 0 km (with respect to the mean sea level) is approx. 350 m/s. For depths larger than 0 km, the average V_s is approx. 500 m/s (Küperkoch et al. 2018).

3.1.2 Recorded data for the greater Munich area

Table 3 lists the earthquakes under consideration for the greater Munich area (G.MUC), encompassing a M_W range from 1.58 to 2.23. For each recording station the most accurate triaxial sensor (E,N,V channels) is selected. Figure 8 shows the distribution of the magnitude of the selected events with respect to the event depth and the distance from the GPP. The geographical locations of the seismic stations and GPPs are illustrated in Fig. 9, while Table 19 in the appendix provides the event-station matrix.

The soil classification corresponds to stiff soil (EC8 - C), with a V_{s30} of approx, 350 m/s. Additional information regarding the events and focal mechanisms can be referenced in the work by Keil et al. (2022).

3.1.3 Simulation data for Munich

Seismic wave simulations for a GPP located in the city center of Munich (MUC) were executed utilizing the SALVUS spectral element code (Afanasiev et al. 2019). The validity of the model was confirmed in earlier studies focusing on Poing, wherein investigations into the 3D subsurface model, parameter uncertainties, and shake maps were undertaken (Keil et al. 2022).

In conducting the simulations, the element size was chosen to control computational costs, ensuring consideration of frequencies up to 10 Hz. A minimum of 1.5 elements per wavelength was employed, with adaptive meshing optimizing the number of elements and grid points in the mesh. For minor earthquakes, the fault was assumed to
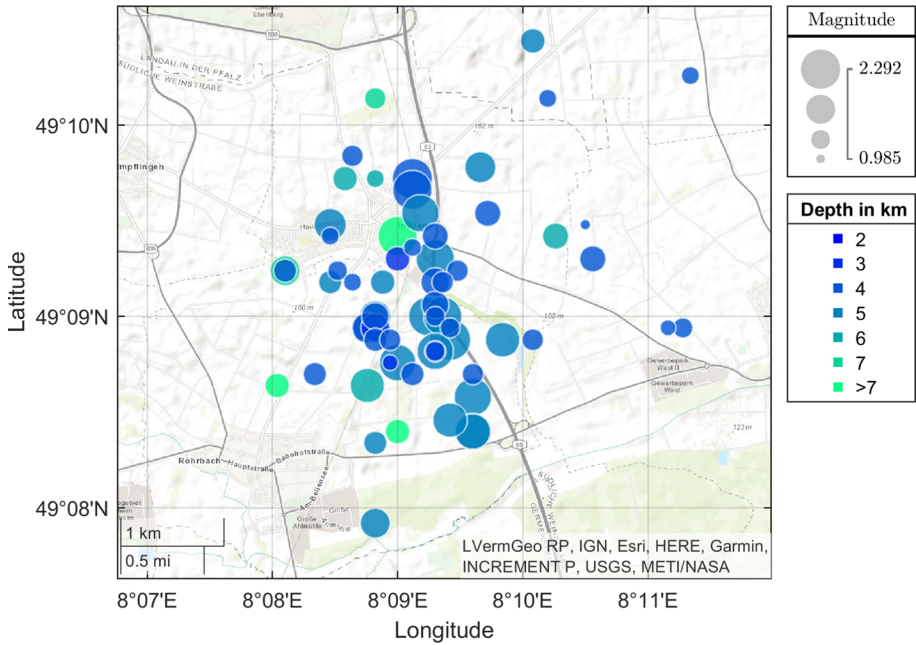
Fig. 6 INS: geographical distribution of the selected events with the corresponding moment magnitude and depth in km

act as a point source with instantaneous rupture. The source time function was represented by a delta pulse, approximated using a sinc-function with a uniform power spectrum up to 10 Hz. Subsequently, the simulated waveforms underwent bandpass filtering between 1 and 10 Hz. It is important to note that the defined frequency range represents an assumption subject to validation and potential adaptation. To verify the impact of the cut-off frequency at 10 Hz, for one selected event with $M_W = 2$, the simulation was repeated with a finer mesh and a cut-off frequency of 20 Hz, which significantly increased the computation costs. The comparison between the results are included in the discussion in Sect. 3.2.

Table 4 provides a summary of the intervals of the seismological characteristics of the 23 simulated earthquakes, while Fig. 30, included in the annex, illustrates the distribution of simulation stations (receivers). The parameters of the simulated events were chosen to reflect the magnitude distribution and depth variations observed in Insheim, where a higher number of recorded events was available. Additionally, we varied the strike and dip to gain further insights. The objective was to achieve a statistical distribution similar to that of the Insheim database.

Figure 10 shows the geographical distribution of the simulated events with the corresponding moment magnitude and depth in km. The site conditions can be regarded as highly similar to other locations in the Greater Munich Area; consequently, variations in site conditions across different locations do not significantly influence the variability of ground motions.
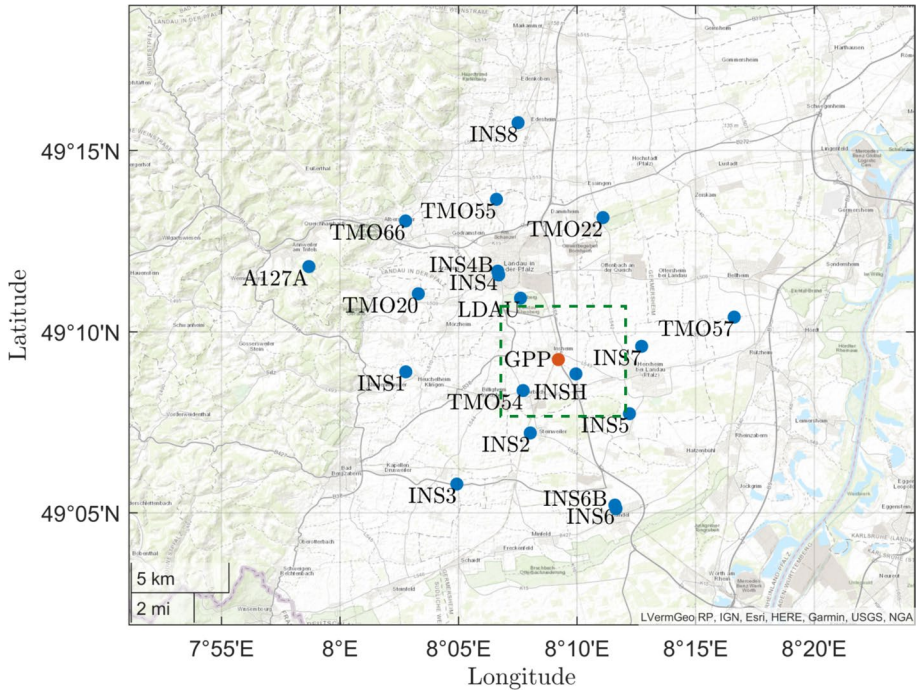
Fig. 7 INS: map of the selected stations for this study (blue dots) and location of the GPP (red dot). The location of the GPP does not coincide with the epicenters of the induced events. The dashed green box represents the area shown in the previous picture, circumscribing the area of the epicenters

3.2 Data elaboration

Subsequently, we will discuss the data elaboration for both measured and simulated data. The ground motions are characterized by several parameters: e.g. magnitude (M_L, M_W), hypocentral distance (r_{hyp}), epicentral distance (r_{epi}), peak ground velocity in horizontal and vertical direction (PGVH, PGVV), peak ground acceleration in horizontal and vertical direction (PGAH, PGAV) and duration. Moreover, for tasks related to the investigation of building vibrations, further quantities are relevant: pseudo acceleration response spectra for the vertical component (SPAV), the geometric mean of the two horizontal components (SPAH), the vertical (SVV) and horizontal (SVH) velocity response spectra. The range of the considered natural periods T spans from 0.01 s to 1 s, corresponding to a natural frequency range of 1-100 Hz. The inclusion of very short periods aims to investigate the associated input frequency content, offering insights into the potential activation of bending modes in walls and ceilings, typically identified between 10 and 40 Hz. To compute the response spectra, a standard damping ratio of the SDOF of 5% has been uniformly applied across the study.

Figure 11 illustrates the distributions of the considered moment magnitude, epicentral distances (r_{epi}), and hypocentral distances (r_{hyp}) across various locations.

In Fig. 12, both the peak ground velocity (PGVH, PGVV) and the peak ground acceleration (PGAH, PGAV) are depicted for all events, stations, and channels, relative to epicentral distance (r_{epi}), for INS. We can conclude that, for the measured magnitudes,

Table 3 Description of the recorded earthquakes in Poing and Unterhaching considered in this study (both in G.MUC)

| Event		Date (dd-mm-yyyy)	Time (hh:mm:ss)	LON (DMS)	LAT (DMS)	D (km)	M_L	M_W	Nr. stations
1	POI	19-Nov-2016	17:41:05	48° 11' 24"	11° 47' 24"	3.9	1.2	1.70	2
2		27-Nov-2016	14:52:21	48° 11' 24"	11° 47' 24"	5.0	1.0	1.58	1
3		07-Dec-2016	05:28:54	48° 11' 24"	11° 47' 24"	6.0	2.1	2.23	4
4		10-Dec-2016	13:38:56	48° 11' 24"	11° 47' 24"	6.6	1.5	1.88	2
5		20-Dec-2016	03:30:51	48° 11' 24"	11° 47' 24"	3.0	1.8	2.05	7
6		09-Sep-2017	17:20:29	48° 11' 24"	11° 47' 24"	3.0	2.1	2.23	8
7	UH	16-Apr-2013	21:51:42	48° 3' 0"	11° 38' 24"	4.7	2.1	2.23	3
8		16-Apr-2013	21:51:48	48° 3' 0"	11° 38' 24"	4.7	2.1	2.23	3
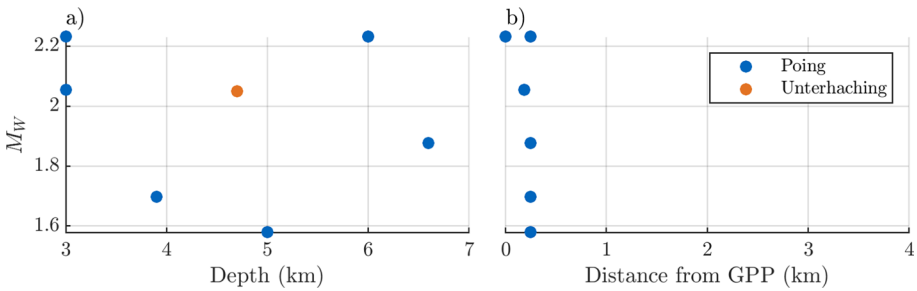
Fig. 8 G.MUC: distribution of the magnitude of the selected events with respect to **a** the event depth in km and **b** the epicentral distance form the GPP in km
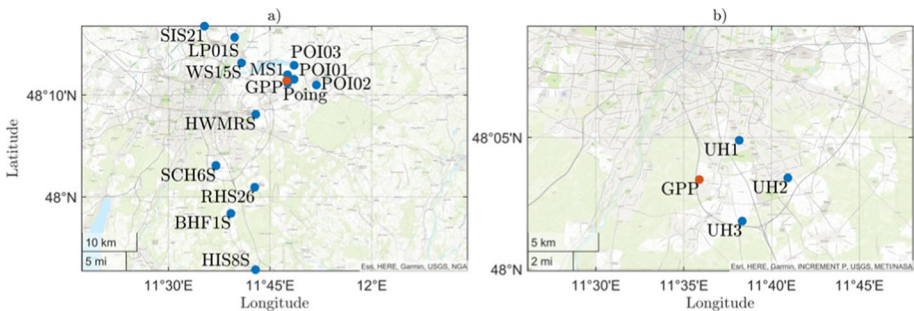
Fig. 9 G.MUC: distribution of the considered stations and the GPPs for **a** poing and **b** unterhaching. The locations of the GPPs do not coincide with the epicenters of the induced events

the ground-motion velocities outside from an epicentral radius of 5 km become unimportant, since the PGVH and PGVV remains below $3 \cdot 10^{-4}$ m/s even for the highest magnitudes. Figures 13 and 14 represent a zoomed-in view for INS and G.MUC respectively, where the range of distances is restricted to $0 \leq r_{epi} \leq 4$ km.

Table 4 Summary of the input parameters for the simulations of the Munich scenarios

Input parameter	Values used for simulations
Epicenters coordinates (GK 31,468, m)	X = [4,466,110, 4,472,884]; Y = [5,330,852, 5,332,327]
Source model	Single point source with a sinc-pulse time function
Seismic Moment (Nm)	[6.3096e+09, 1.7783e+13]
Stress drop parameter (bars)	[20, 50]
Attenuation κ (s)	0.04
Density (kg/m)	Varies between 2300 and 2900
V_S (m/s)	Increases from 350 to 3526 over 5 km depth
V_P (m/s)	Increases from 1050 to 6100 over 5 km depth
M_W	[0.5, 2.8]
Depth (km)	[3.02, 4.0]
Strike (°)	[55, 75]
Dip (°)	[78, 80]
Rake (°)	− 15
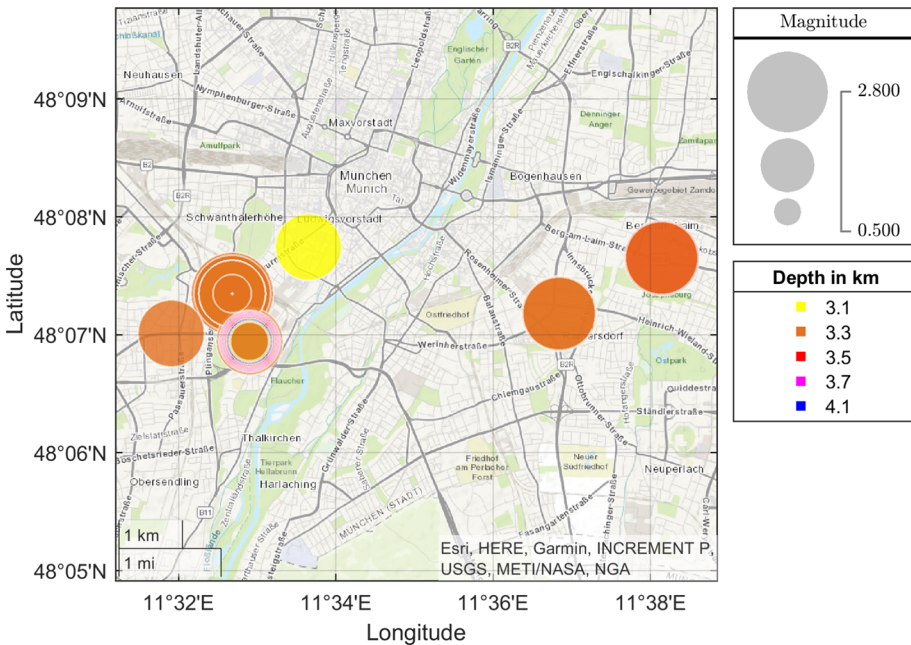
Fig. 10 Munich (simulations): geographical distribution of the simulated events with the corresponding moment magnitude and depth in km

Typically, GMPEs presuppose that the logarithm of spectral quantities diminishes with the logarithm of the epicentral distance. However, it becomes evident that, at very short distances for $r_{epi} \leq 4$ km, this trend is not applicable. As demonstrated statistically in a previous study (Keil et al. 2022), the scatter plots reveal that PGV and PGA tend to remain relatively constant (near-source saturation) or experience a slight increase with

Fig. 11 Distributions of M_W, epicentral distances and hypocentral distances for all signals (all directions) and locations. Columns **a**, **b** and **c** from observations and column **d** from simulations
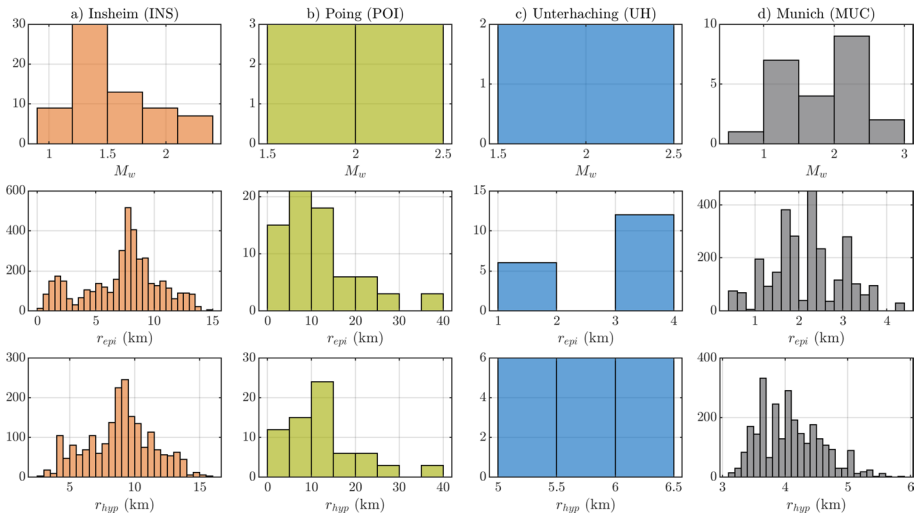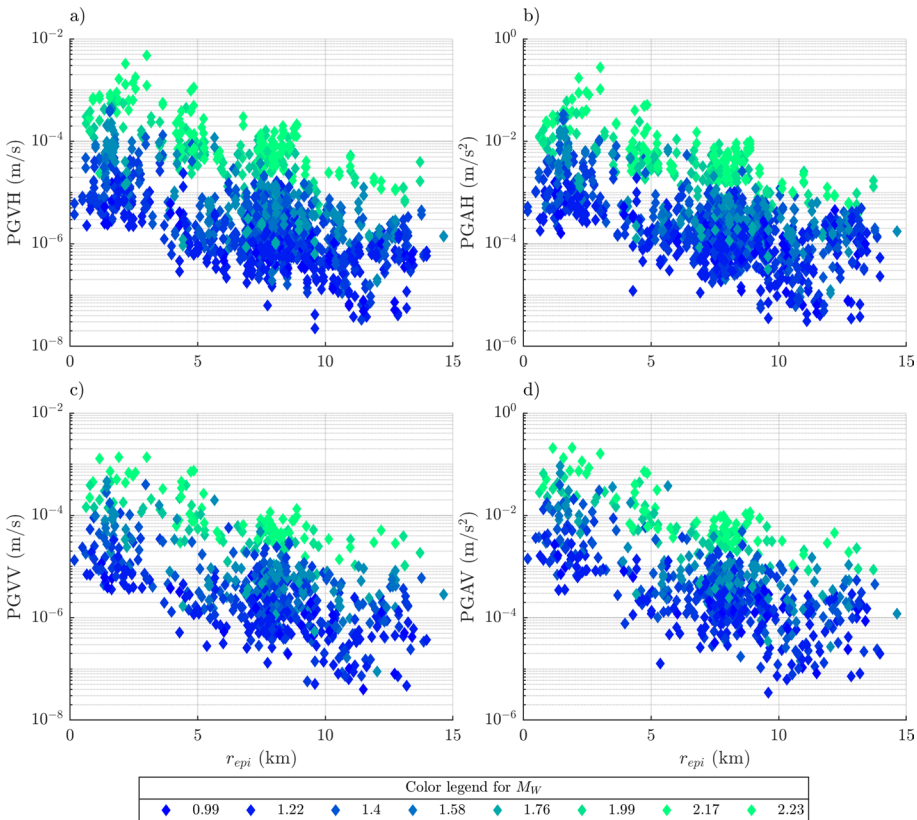

Fig. 12 INS: **a** PGVH, **b** PGAH, **c** PGVV and **d** PGAV for all locations, events, stations, and channels as a function of the r_{epi}

distance up to approximately $r_{\mathrm{epi}} = 2.5$ km. Beyond this threshold, a rapid decrease is observed for larger distances.

For the simulated event with the highest moment magnitude ($M_W = 2.8$), the PGVH surpasses values of 10 mm/s. This exceeds the established limit (5 mm/s) for maximum ground velocities specified by the German standard DIN 4150-3 (DIN 2016) to prevent potential cosmetic damage to standard residential buildings. However, when addressing structural vibrations, it becomes crucial to explore spectral quantities rather than focusing solely on absolute maximum values.

Conventionally, spectral quantities have been commonly estimated as pseudo-spectral quantities, derived from the spectral displacement of a single-degree-of-freedom (SDOF) system under the assumption of harmonic oscillations. This represents a notable approximation, given that seismic signals are inherently non-harmonic. It can be demonstrated that, for accelerations, this approximation is deemed acceptable at short natural periods within the acceleration-sensitive range. Moreover, most of the available GMPEs are given in terms of pseudo spectral accelerations in horizontal direction. Consequently, the comparison between ground motion data and existing GMPE models is executed using SPAH (see Sect. 4).

However, when it comes to velocities at short natural periods, relying on the pseudo-velocity approximation may lead to significant overestimation errors, as indicated in Samdaria and Gupta (2018). Hence, no such approximation is employed for velocities.

Figures 15 and 16 illustrate horizontal (SPAH) and vertical (SPAV) pseudo spectral accelerations, respectively, in relation to the period and various bins of moment magnitude and hypocentral distance. The magnitude range is confined to recorded values, specifically $1.5 \leq M_W \leq 2.3$. The data are distributed in bins of M_W and r_{hyp}. The columns of plots refer to the same bin of magnitudes, left for $1.5 \leq M_W < 1.9$ and right for $1.9 \leq M_W \leq 2.3$; and the rows of plots correspond to the same bin of hypocentral distances, increasing from top to bottom. Distinct colors are assigned to different locations, with continuous lines representing the mean curve for each location and bin, and dotted lines indicating individual samples within each bin. The four numbers in each subplot denote the sample count for each bin and location, corresponding to the respective color. The data are compared to 3 existing GMPEs and the discussion of this comparison proceeds in Sect. 4.1.

In general, the station-to-station variability (maximum distance between samples) for a single location within one bin can be on the order of 10. In cases where multiple samples are available for various locations within a bin, it can be inferred that the variability stemming from site effects (at different locations) falls within the range of station-to-station variability for a single location. Figures 17 and 18 illustrate the same plots for the horizontal (SVH) and vertical (SVV) spectral velocities, respectively. Here, no comparison with existing GMPEs was possible, as models for spectral velocities are not available.

For periods exceeding 0.1 s, the simulation data aligns with the variability observed in the recorded data. Below 0.1 s, the simulated data exhibit a sharp drop in amplitude due to the imposed cutoff frequency at 10 Hz. Notably, for SVV, the highest values are observed between 0.05 s and 0.1 s, indicating significant input spectral content between 10 and 20 Hz. In contrast, SVH exhibits maxima above 0.1 s. Consequently, it is apparent (especially from Fig. 18) that the simulated data can only be utilized for calibrating GMPEs for horizontal oscillations.

Figure 19 shows a comparison between the simulation results with a cut-off frequency of 10 Hz and 20 Hz in terms of spectral velocities at two different r_{epi}. In general, the simulation curves differ due to variations in discretization size and corresponding frequency resolution, which affect the wave propagation process. However, focusing on panel a) and

Fig. 13 INS: **a** PGVH, **b** PGAH, **c** PGVV and **d** PGAV for all locations, events, stations, and channels as a function of the r_{epi}, at very short distances

the frequency range of interest between 2 and 50 Hz (indicated by green dashed lines), we observe a maximum difference between the two curves of a factor of 2.5 for $T \geq 0.1s$. This falls within the station-to-station variability factors of the observations, and can therefore be considered acceptable. For $T < 0.1$, the difference factor between the two curves increases significantly, with peaks around 30, where the 10-Hz cut-off leads to an underestimation of the spectral velocities. This discrepancy is particularly significant for the vertical component, where frequency content up to 40 Hz can play a crucial role in building vibrations.

4 GMPE

4.1 Existing models

Previous studies have shown the substantial inherent variability in ground motion data from small earthquakes and the challenges in favoring particular models over others (Douglas et al. 2013). Therefore, before introducing the newly developed GMPE, we conducted a

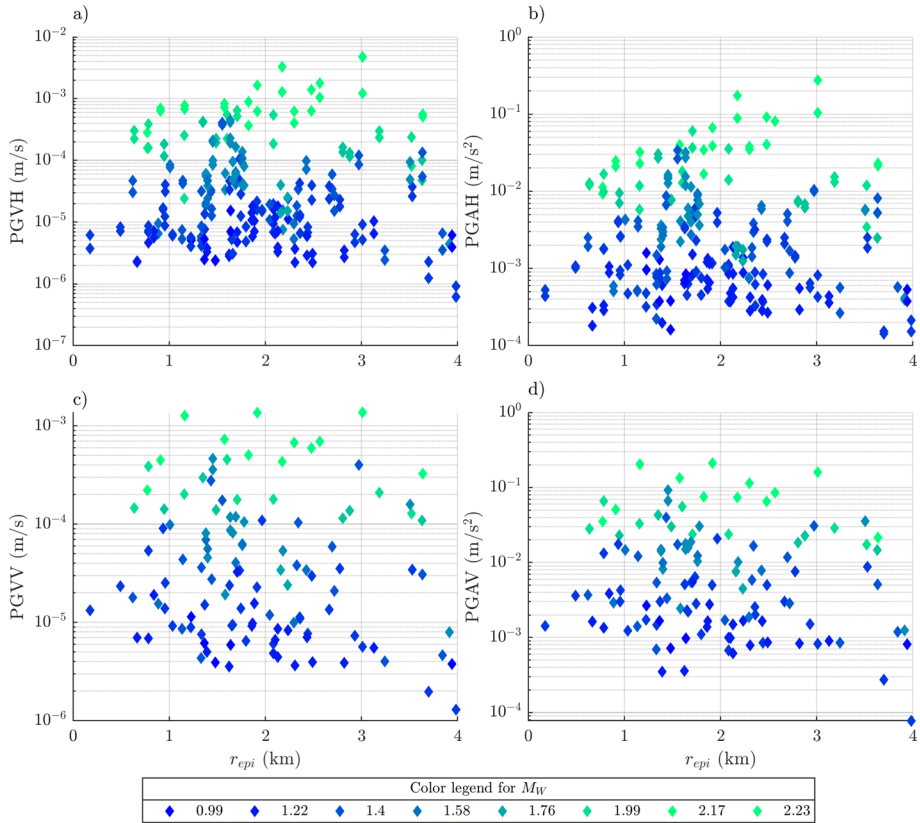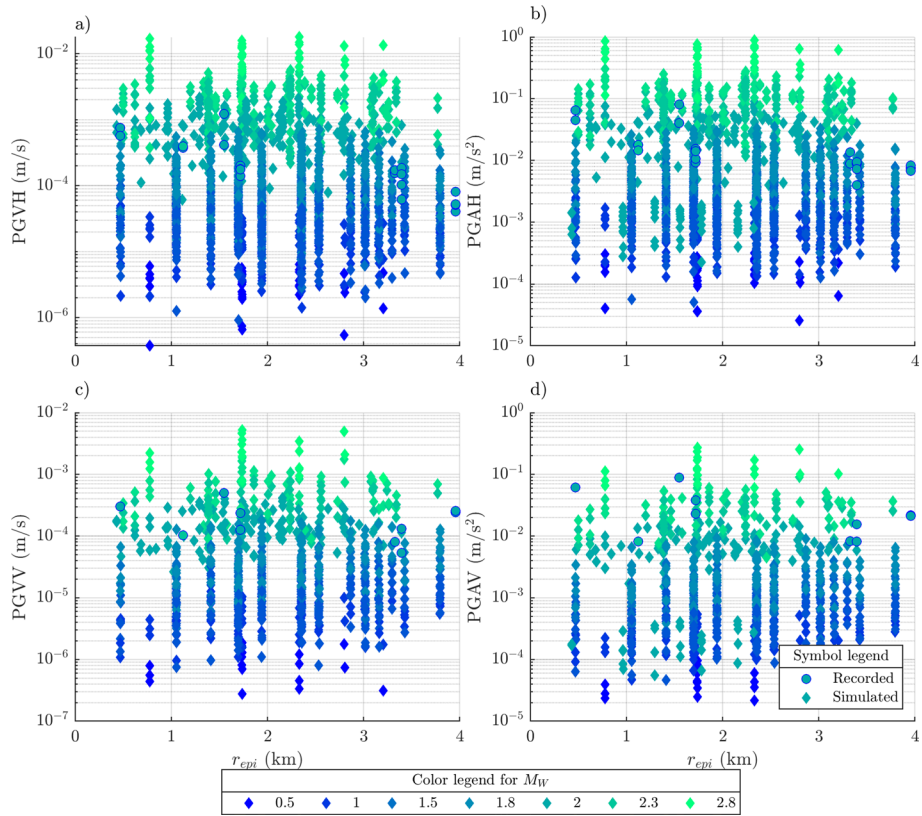**Fig. 14** G.MUC: **a** PGVH, **b** PGAH, **c** PGVV and **d** PGAV for all locations, events, stations, and channels as a function of the r_{epi}, at very short distances. Different markers identify recorded and simulated data

comparison with existing models to guide the selection of the appropriate backbone curve. Three existing models - DGL (Douglas et al. 2013), ATK (Atkinson 2015), and KHS (Khansefid et al. 2023) - were considered. The respective functional forms are provided in Table 5, and the corresponding coefficients can be referenced in the cited sources. The errors ε are assumed to be independent and identically distributed, with zero-mean and standard deviation σ.

The DGL model (Douglas et al. 2013) is based on a generic stochastic model suitable for shallow earthquakes with magnitudes ranging from 1 to 5, specifically in close proximity ($r_{hyp} < 50$ km). They generated 36 GMPE models to encompass various stress-drop and attenuation scenarios, spanning combinations of Q values (200, 600, and 1800), Brune's stress parameter $\Delta\sigma$ (1, 10, and 100 bar), and κ values (0.005, 0.02, 0.04, and 0.06 s). In the present study, the magnitudes of the available data only covers the range of $0.5 \leq$ Mw ≤ 2.3, and over this range the effect of $\Delta\sigma$ is limited. Consequently, we only consider a single stress parameter (10 bar). Most of the records are from narrow distances, and consequently, it was not possible to determine Q, which was assumed to be equal to 1800 (low attenuation). Therefore, we reduced the 36 potential GMPEs to four models, specifically those with κ values of 0.005, 0.02, 0.04, and 0.06. An important aspect in the DGL model, is that there is high variability in the observation at very short natural periods

Fig. 15 Trellis plots comparing the observed SPAH in g at different locations and different existing models. Distinct colors are assigned to different locations, with continuous lines representing the mean curve for each location and bin, and dotted lines indicating individual samples within each bin. See description in text
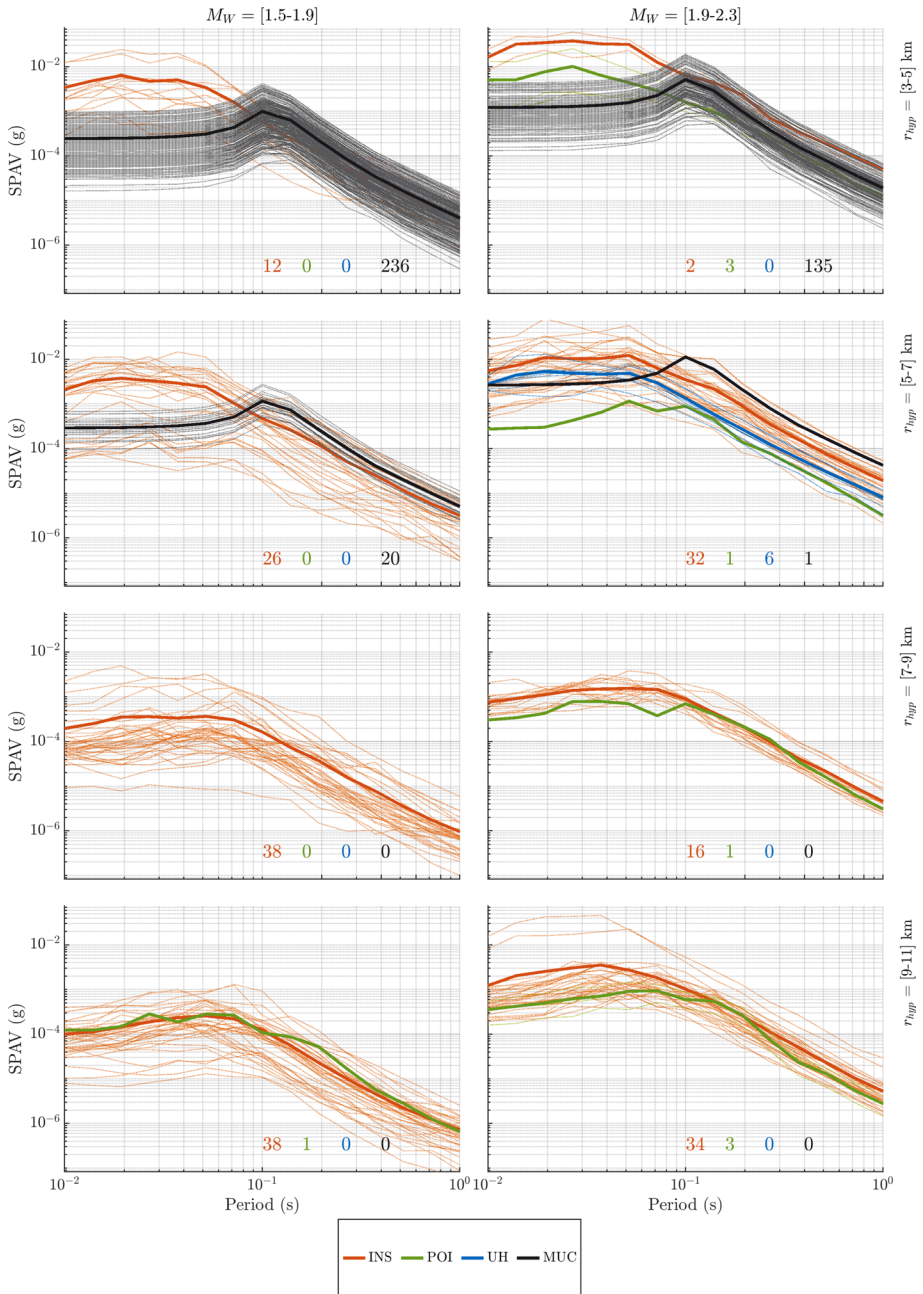
Fig. 16 Trellis plots comparing the observed SPAV in g at different locations and different existing models. Distinct colors are assigned to different locations, with continuous lines representing the mean curve for each location and bin, and dotted lines indicating individual samples within each bin. See description in text
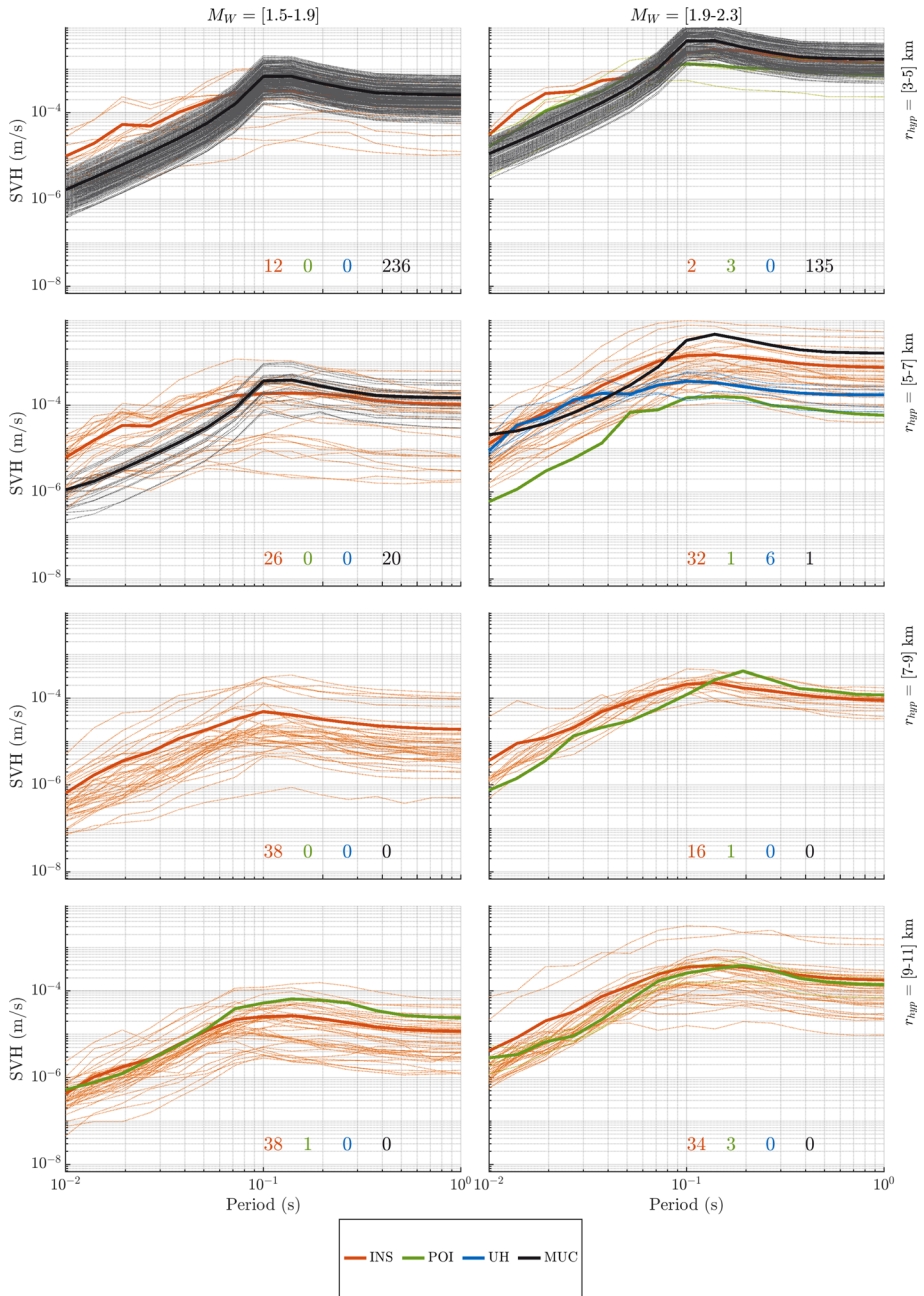
Fig. 17 Trellis plots comparing the observed SVH in m/s at different locations and different existing models. Distinct colors are assigned to different locations, with continuous lines representing the mean curve for each location and bin, and dotted lines indicating individual samples within each bin. See description in text
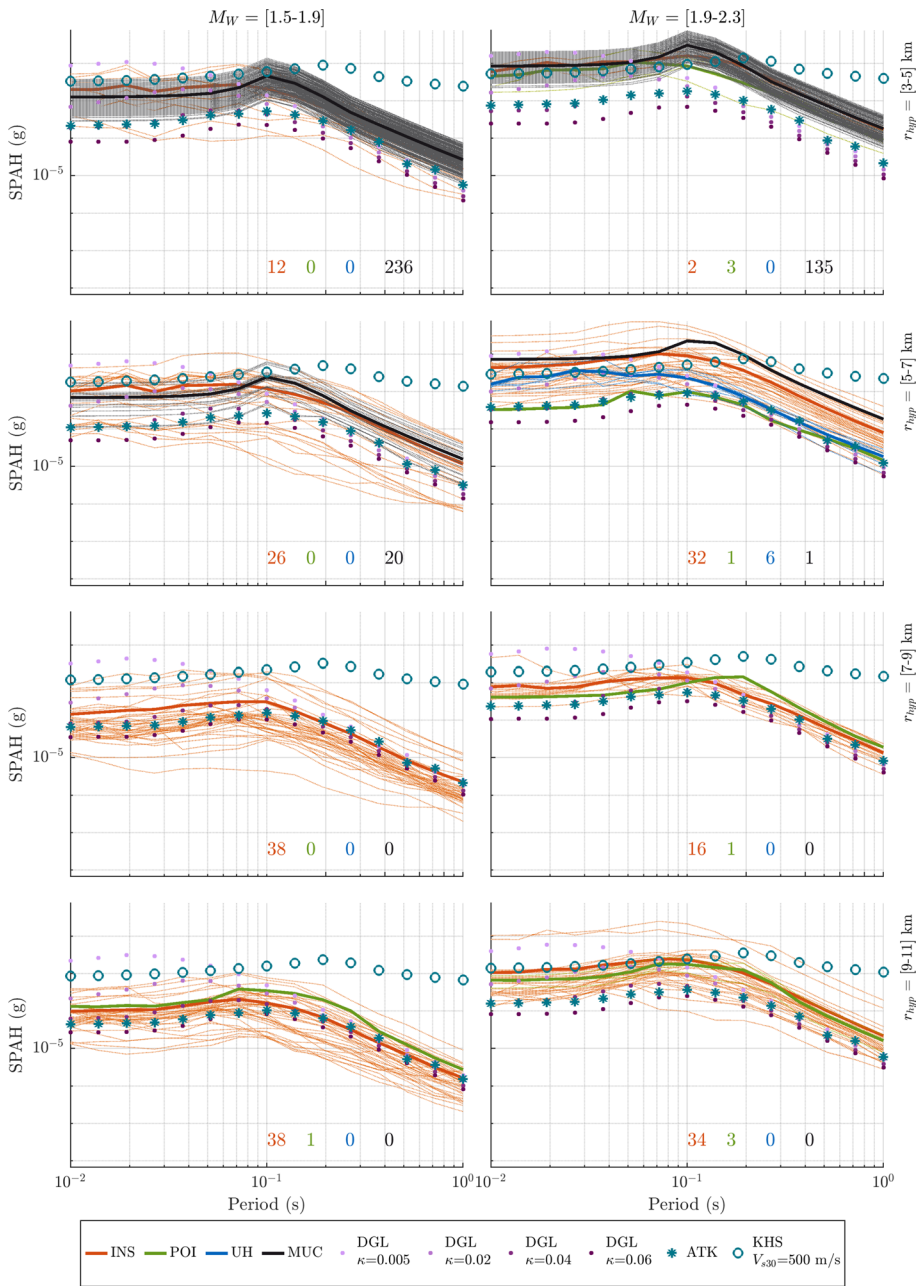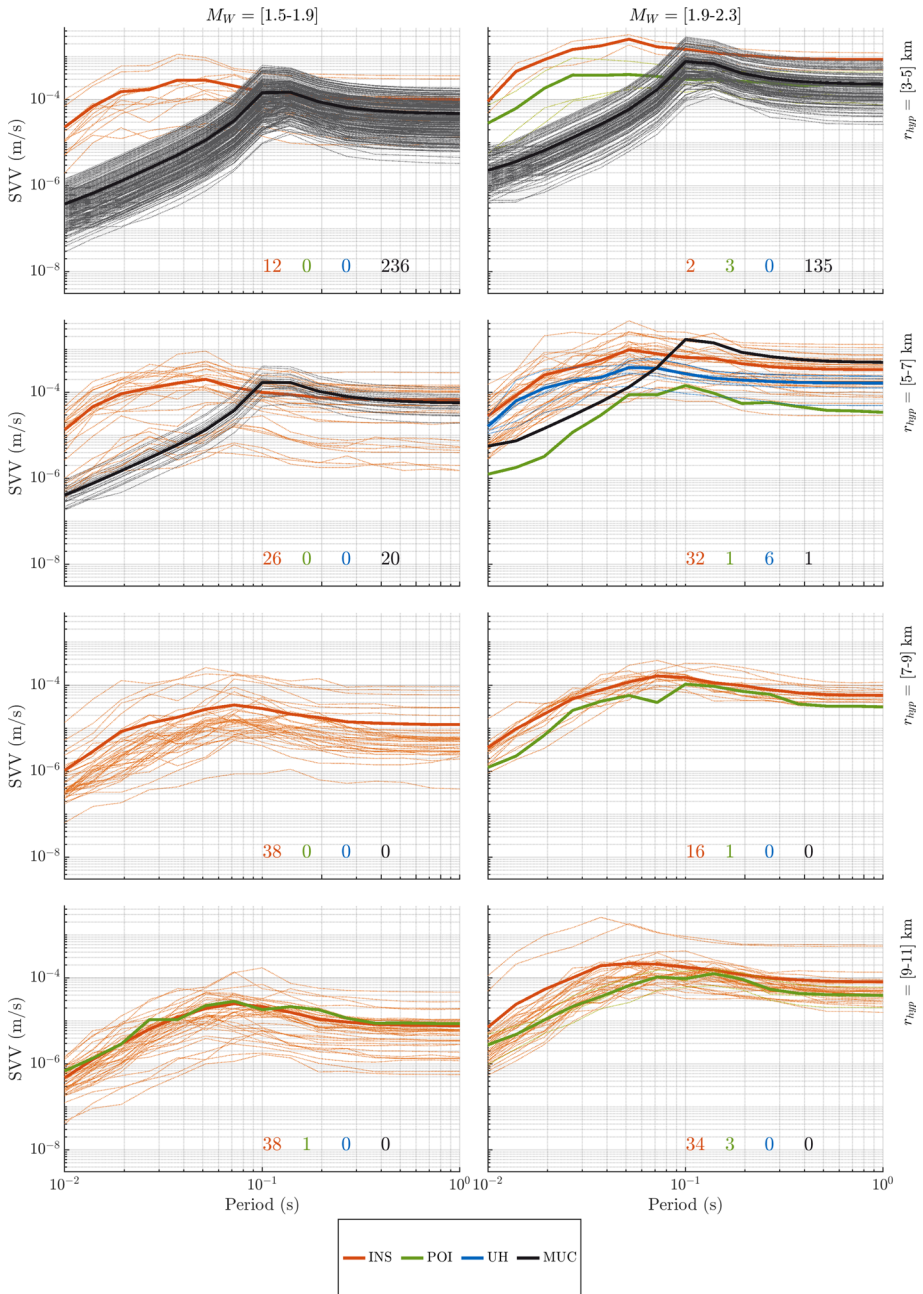
Fig. 18 Trellis plots comparing the observed SVV in m/s at different locations and different existing models. Distinct colors are assigned to different locations, with continuous lines representing the mean curve for each location and bin, and dotted lines indicating individual samples within each bin. See description in text
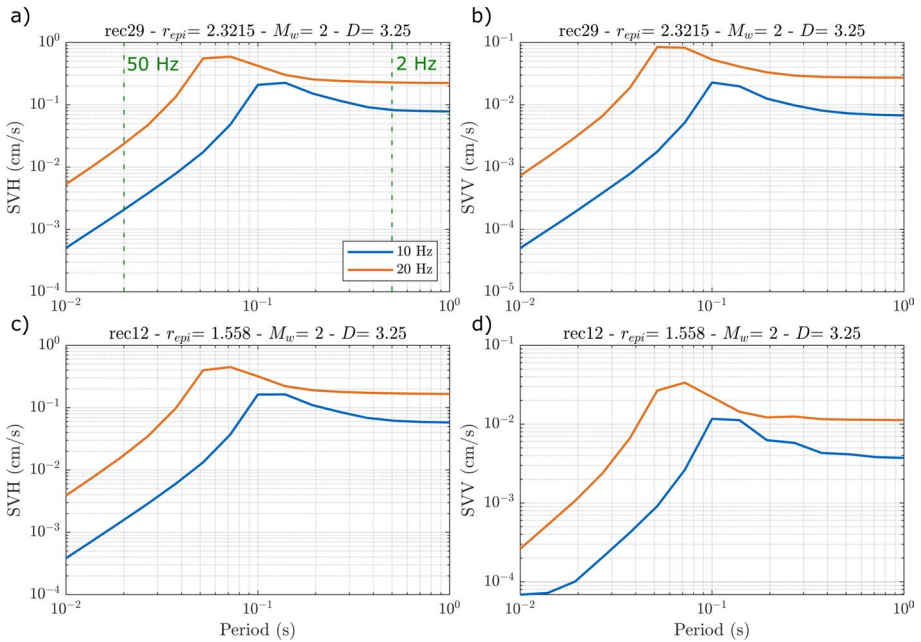
Fig. 19 Comparison between the simulation results with a cut-off frequency of 10 Hz and 20 Hz, for $M_W = 2$. Panels **a** and **b** refer to a $r_{epi} = 2.3$ km and show the SVH and SVV respectively; panels **c** and **d** refer to a $r_{epi} = 1.6$ km and show the SVH and SVV respectively. The event depth D is given in km

Table 5 Considered functional forms from existing GMPEs and proposed function

DGL 2013 (Douglas et al. 2013)

$$\ln(Y) = \beta_1 + \beta_2 (M_W - 3) + \beta_3 (M_W - 3)^2 \qquad (2)$$
$$+ \beta_4 (M_W - 3)^3 + \beta_5 \ln (r_{hyp} + \beta_h) + \beta_6 (r_{hyp} + \beta_h) + \varepsilon$$

ATK 2015 (Atkinson 2015)

$$\log(Y) = \beta_1 + \beta_2 M_W + \beta_3 M_W^2 + \beta_4 \log(r) + \varepsilon \qquad (3)$$

with $r = \sqrt{r_{hyp}^2 + h_{eff}^2}$ and $h_{eff} = \max (1, 10^{(-0.28 + 0.19 M_W)})$

KHS 2023 (Khansefid et al. 2023)

$$\ln(Y) = \beta_1 + \beta_2 M_W + \beta_3 \ln (r_{hyp}) + \beta_4 \ln (V_{s30}) + \varepsilon \qquad (4)$$

Proposed function

$$\log(Y) = \beta_1 + \beta_2 M_W + \beta_3 \log(r) + \varepsilon \qquad (5)$$

with $r = \sqrt{r_{hyp}^2 + h_{eff}^2}$ and $h_{eff} = \max (0.5, 10^{(-0.28 + 0.19 M_W)})$

(higher natural frequencies). This aspect was integrated into the 36 empirical models as aleatory variability, rather than being treated as epistemic uncertainty in the values of $\Delta\sigma$, κ, and Q. The spectral variability at higher frequencies is important when addressing serviceability and comfort issues in buildings, because they arise from the bending vibrations

of walls and ceilings and are connected to amplification in the frequency range of 10 to 30 Hz ($T = [0.03\, s - 0.1\, s]$). Moreover, the site condition for the DGL model is assumed to be rock with a V_{s30} of approx. 1100 m/s, which is stiffer than the conditions for INS and G.MUC.

The ATK model (Atkinson 2015) distinguishes itself from other models through the incorporation of the term h_{eff}, representing the distance-saturation effect. This signifies the average distance along the strike of the fault to the asperity responsible for the motion. For smaller events, this distance is assumed to be less than 1 km. At very close distances, the ATK model predicts higher amplitudes than the DGL model. The site conditions are assumed to be for a soft rock with V_{s30} of approx. 760 m/s.

The KHS model (Khansefid et al. 2023) presents a simpler form with a linear dependence on M_W. It is developed from a worldwide database and contains a term for the consideration of different site conditions. For the comparison we assume here $V_{s30} = 500$ m/s.

In the following, we extend the discussion from Sect. 3.2, considering again Figs. 15, 16, 17 and 18. The existing models are shown with different markers. The three considered models are compared against the data, revealing a notable disparity with factor greater than 10, particularly at shorter periods. For the SPAV, the data are compared to the model for horizontal spectral accelerations, as in the existing models no separated regression is done for the vertical direction. While the KHS model better aligns with the data for periods below 0.1 s, it exhibits lower accuracy for larger periods, likely due to its development for earthquakes with magnitudes ranging from 2.5 to 5.4 and reliance on actual spectra acceleration instead of pseudo values. The ATK and DGL models closely track each other for κ between 0.06 and 0.04, following the data trend well but consistently providing lower values than the mean of observations.

The three existing models under consideration assume different soil conditions: DGL assumes a V_{s30} of 1100 m/s, ATK assumes 760 m/s, and KHS assumes 500 m/s. The KHS model allows for variation in soil conditions and testing different values other than 500 m/s yielded very small differences (not shown here). Atkinson (2015) compared her model with the one of Douglas et al. (2013) under the specified site conditions and did not cite differing soil conditions as a source of model discrepancy. This suggests that site conditions for rather stiff soils are not a predominant parameter affecting discrepancies between models. However, site conditions can still play a role when comparing models with observations, especially if amplification correction techniques are used, as in the considered existing models. In general, results may differ significantly for very soft soil, with a V_{s30} below 200 m/s, but this scenario does not apply to the considered models and/or the observations from Insheim and the Greater Munich area.

Based on the model comparison, we propose a functional form, given in Eq. 5, combining features from the KHS and ATK models. It is essential to note that we choose a minimum value of 0.5 km for h_{eff} instead of 1 km, driven by the assumption that, for the considered magnitude, the fault size is smaller than in the ATK study.

It must be noted, that for short distances ($r_{\text{hyp}} = [3 - 5]$ km) and for the largest recorded magnitudes (for example the upper panels in Fig. 16), the data exhibit a notable spectral contribution for periods < 0.1 s, with discrepancies reaching up to a factor of 10 compared to existing models. This will be reflected also in the regression curves and discussed in the next section.

Table 6 Coefficients for peak ground quantities in cm/s^2 and cm/s, with Φ_{j1} for INS and Φ_{j2} for G.MUC (INS, POI and simulations for MUC) and $j = 1, 2, 3$

	β_1	β_2	β_3	σ	Φ_{11}	Φ_{21}	Φ_{31}	Φ_{12}	Φ_{22}	Φ_{32}
PGAH	−1.354	1.608	−2.29	0.331	−1.354	1.657	−2.675	−1.354	1.558	−1.906
PGAV	−0.924	1.367	−2.186	0.476	−0.924	1.777	−3.178	−0.924	0.957	−1.194
PGVH	−3.286	1.798	−2.547	0.325	−3.852	2.07	−2.741	−2.721	1.526	−2.354
PGVV	−3.859	1.903	−2.544	0.45	−3.794	1.903	−2.544	−3.924	1.903	−2.544

4.2 Regression with mixed-effects

In this section we present the result of the regression based on the linear mixed-effects (LME) approach (Abrahamson and Youngs 1992). For each seismic quantity (PGAH, PGAV, PGVH, PGVV, SPAH, SPAV, SPVH, SPVV, SVH, SVV), the regression is performed by grouping the data into 2 regions: Insheim (INS) and the Greater Munich Area (G.MUC), comprising the locations Poing, Unterhaching and Munich (simulated). Like all regression models, their purpose is to characterize a response variable in terms of predictor (independent) variables, e.g. M_W and r_{hyp}. Mixed-effects models, however, acknowledge correlations within sample subgroups (here the two regions, INS and G.MUC), striking a balance between disregarding data groups entirely, resulting in the loss of valuable information, and fitting each group separately, which necessitates a considerably larger number of data points. For the quantities in horizontal direction all recorded and simulated data are used. In vertical directions, the simulated data with a cut-off frequency of 10 Hz are removed from the dataset (only one event with cut-off frequency of 20 Hz is kept), as explained in sec. 3.2.

The LME approach accommodates individual region-specific variations through random effects, linking different individuals via fixed effects and a variance-covariance matrix.

Through the LME, Eq. (5) is extended into the system Eqs. (6–9). The magnitude M can take the values of either M_W or M_L. The fixed-effects coefficients β_i represent mean values in the population of individual data points. Regional deviations are captured by random effects b_{ji}, assumed to follow a normal distribution with a variance-covariance matrix $\mathbf{\Psi}$. As the random effects for different regions (INS or G.MUC) are assumed to be independent, the variance-covariance matrix is equal to a diagonal matrix containing the variances for the three random-effects parameters. The errors ε are assumed to be independently distributed as $N(0, \sigma^2)$ and are independent of the random effects.

$$\log \mathbf{Y} = \Phi_{1i} + \Phi_{2i}M + \Phi_{3i}\log r_{\text{hyp}} + \varepsilon \, , \tag{6}$$

$$\mathbf{\Phi}_i = \begin{bmatrix} \Phi_{1i} \\ \Phi_{2i} \\ \Phi_{3i} \end{bmatrix} = \underbrace{\begin{bmatrix} \beta_1 \\ \beta_2 \\ \beta_3 \end{bmatrix}}_{\text{fixed effects}} + \underbrace{\begin{bmatrix} b_{1i} \\ b_{2i} \\ b_{3i} \end{bmatrix}}_{\text{random effects}} = \beta + \mathbf{b}_i \text{ with } i = 1(\text{INS}), 2(\text{G.MUC}) \, , \tag{7}$$

$$\mathbf{b}_i \sim \mathcal{N}(N, \mathbf{I}\sigma_{bi}^2), \tag{8}$$

Table 7 Coefficients for SPAH in cm/s², with Φ_{j1} for INS and Φ_{j2} for G.MUC (INS, POI and simulations for MUC) and $j = 1, 2, 3$

f (Hz)	T (s)	β_1	β_2	β_3	σ	Φ_{11}	Φ_{21}	Φ_{31}	Φ_{12}	Φ_{22}	Φ_{32}
100	0.01	−0.998	1.482	−2.272	0.331	−0.704	1.413	−2.631	−1.291	1.551	−1.912
71.43	0.014	−1.052	1.558	−2.374	0.326	−0.858	1.558	−2.755	−1.246	1.558	−1.993
52.63	0.019	−1.096	1.626	−2.472	0.332	−0.991	1.684	−2.862	−1.2	1.568	−2.082
37.04	0.027	−1.219	1.676	−2.417	0.322	−1.219	1.779	−2.791	−1.219	1.572	−2.043
27.03	0.037	−1.193	1.733	−2.504	0.333	−1.193	1.885	−2.94	−1.193	1.581	−2.067
19.23	0.052	−1.235	1.786	−2.51	0.344	−1.433	1.978	−2.77	−1.036	1.594	−2.25
13.89	0.072	−1.107	1.801	−2.595	0.337	−1.401	2.03	−2.858	−0.814	1.571	−2.332
10	0.1	−1.008	1.818	−2.664	0.333	−1.778	2.118	−2.664	−0.237	1.519	−2.664
7.19	0.139	−1.305	1.84	−2.537	0.327	−2.029	2.175	−2.687	−0.581	1.505	−2.388
5.18	0.193	−1.754	1.841	−2.33	0.315	−2.398	2.173	−2.542	−1.11	1.51	−2.118
3.73	0.268	−2.17	1.802	−2.134	0.305	−2.644	2.09	−2.412	−1.696	1.515	−1.857
2.68	0.373	−2.487	1.749	−2.039	0.293	−2.937	1.981	−2.228	−2.036	1.517	−1.85
1.93	0.518	−2.717	1.695	−2.039	0.288	−3.096	1.87	−2.194	−2.337	1.52	−1.885
1.39	0.72	−2.928	1.635	−2.019	0.286	−3.17	1.746	−2.207	−2.687	1.523	−1.83
1	1	−3.101	1.557	−1.984	0.291	−3.119	1.579	−2.261	−3.083	1.535	−1.707

$$\varepsilon \sim \mathcal{N}(0, \sigma^2). \tag{9}$$

Table 6 gives the coefficients for peak ground quantities, with respect to M_W. Users can consult the fixed-effects coefficients for a general model and/or employ region-specific projections for risk assessment in local projects. Figure 20 shows the regression curves for the PGVH for four magnitude bins (with different colors) as a function of the r_{hyp}. Solid lines represent the fixed-effects estimators, while dashed lines with markers correspond to the region-specific random-effects models. The regressions are compared to both recorded and simulated data points. The residuals, which are the logarithm of the rations between observed and predicted quantities, consistently fall within the range of [−1.5, 1.5] and exhibit no discernible trends, indicating the appropriateness of the chosen functional form. Similar results are obtained for all the quantities. Figure 21 shows that the fixed-effects regression for the vertical direction is similar to the horizontal case, the random effects are less evident, leading to very similar trends with respect to to r_{hyp} for the two regions. Figures 22 and 23 show the regression curves for the spectral velocities at $T = 0.1$ s in horizontal and vertical direction respectively.

Tables 7, 8, 9 and 10 give the regression coefficients for the remaining spectral quantities, with respect to M_W. In these tables, the symbols Φ_{ji} indicate the expected values of the corresponding random quantities in Eq. (7). Regression coefficients with respect to M_L are provided as described in Data and Resources.

Further plots for the PGAV are given in the annex, in Figs. 31 and 32.

Figure 24 displays regression curves for SPAH (in g) as a function of the period, in comparison to existing models across various magnitudes and distances, using a linear scale for clarity. It is confirmed that for larger magnitudes, the proposed curves yield higher values for periods < 0.1 s, with discrepancies against existing models reaching up to a factor of 10. This aligns with the behavior observed in the data. The increased amplitude at short periods predominantly influences the modal contribution in the vertical direction, where

Table 8 Coefficients for SPAV in cm/s^2, with Φ_{j1} for INS and Φ_{j2} for G.MUC (INS, POI and simulations for MUC) and $j = 1, 2, 3$

f (Hz)	T (s)	β_1	β_2	β_3	σ	Φ_{11}	Φ_{21}	Φ_{31}	Φ_{12}	Φ_{22}	Φ_{32}
100	0.01	−0.276	1.07	−2.18	0.479	−0.276	1.475	−3.154	−0.276	0.665	−1.205
71.43	0.014	−0.096	1.129	−2.438	0.487	−0.096	1.642	−3.6	−0.096	0.615	−1.276
52.63	0.019	−0.232	1.29	−2.583	0.493	−0.232	1.827	−3.738	−0.232	0.753	−1.428
37.04	0.027	−0.743	1.542	−2.532	0.476	−0.743	1.993	−3.43	−0.743	1.091	−1.633
27.03	0.037	−1.229	1.763	−2.456	0.483	−1.229	2.08	−3.04	−1.229	1.445	−1.873
19.23	0.052	−1.439	2.023	−2.797	0.495	−1.439	2.071	−2.797	−1.439	1.974	−2.797
13.89	0.072	−1.662	1.934	−2.492	0.483	−1.662	1.983	−2.492	−1.662	1.886	−2.492
10	0.1	−2.156	1.891	−2.118	0.463	−2.156	1.945	−2.118	−2.156	1.838	−2.118
7.19	0.139	−2.726	1.923	−1.886	0.436	−2.726	1.973	−1.886	−2.726	1.874	−1.886
5.18	0.193	−3.101	1.905	−1.789	0.424	−3.042	1.905	−1.789	−3.159	1.905	−1.789
3.73	0.268	−3.226	1.749	−1.655	0.407	−3.226	1.749	−1.655	−3.226	1.749	−1.655
2.68	0.373	−3.24	1.618	−1.724	0.414	−3.24	1.618	−1.724	−3.24	1.618	−1.724
1.93	0.518	−3.432	1.491	−1.528	0.415	−3.038	1.491	−2.013	−3.826	1.491	−1.043
1.39	0.72	−3.478	1.373	−1.54	0.418	−3.027	1.373	−2.107	−3.929	1.373	−0.972
1	1	−3.581	1.258	−1.472	0.432	−3.098	1.258	−2.101	−4.064	1.258	−0.843

the pertinent natural frequencies are within the lower period range. Horizontal vibrations are less impacted, as typical global bending modes in horizontal directions exhibit natural periods above 0.1 s. Figure 25 shows the SVH and SVV in m/s. As observed in the data, also the proposed regression curves confirm that the period range for maximum vertical vibrations is shifted to a lower value with respect to the horizontal vibrations.

In Fig. 25, one can also observe that for smaller magnitudes, the GMPE for SVH for G.MUC is higher than that for INS. For intermediate magnitudes, they are comparable, while for larger magnitudes, the trend reverses. Interpreting this aspect is challenging, particularly due to the lack of actual recordings at low magnitudes for G.MUC. In the horizontal direction, the use of physics-based data (23 events with a cut-off frequency of 10 Hz) to compensate for the scarcity of low-magnitude recordings may contribute to this effect. In the vertical direction only one simulated event with $M_W = 2$ and a cut-off frequency of 20 Hz was used and this phenomenon is not evident. It is difficult to determine whether this effect arises from the use of physics-based data at low magnitudes or other factors, such as the seismological process itself. The seismological process for G.MUC might differ from that in INS, as the GPPs have different characteristics and can therefore exhibit different relationships between maximum spectral velocities and increasing magnitude. This aspect can only be thoroughly investigated once more recordings at low magnitudes (e.g. 5 new events with $M_W > 1.5$) become available for G.MUC.

5 Example of application

In this illustration, we apply spectral velocities derived from the estimator in Eqs. (6) and (7) for a varying M_W, $D = 4$ km, $r_{epi} = 3$ km, and $r_{hyp} = 5$ km. To select the parameters, we aimed to represent the "worst-case" scenario. According to Keil et al. (2022), shake maps for G.MUC for various events with local magnitudes between 1.8 and 2.1 indicated that the area experiencing the largest ground motion is located approximately 2.5 km south of the epicenter.

Table 9 Coefficients for SVH in cm/s, with Φ_{j1} for INS and Φ_{j2} for G.MUC (INS, POI and simulations for MUC) and $j = 1, 2, 3$

f (Hz)	T (s)	β_1	β_2	β_3	σ	Φ_{11}	Φ_{21}	Φ_{31}	Φ_{12}	Φ_{22}	Φ_{32}
100	0.01	−4.604	1.341	−1.854	0.352	−3.436	1.084	−2.707	−5.773	1.598	−1.001
71.43	0.014	−4.298	1.448	−2.102	0.354	−3.247	1.296	−2.959	−5.349	1.601	−1.245
52.63	0.019	−4.063	1.525	−2.23	0.359	−3.183	1.454	−3.039	−4.942	1.596	−1.421
37.04	0.027	−4.019	1.615	−2.207	0.342	−3.477	1.615	−2.812	−4.56	1.615	−1.601
27.03	0.037	−3.798	1.72	−2.351	0.35	−3.505	1.831	−2.867	−4.092	1.609	−1.835
19.23	0.052	−3.589	1.783	−2.404	0.363	−3.589	1.947	−2.707	−3.589	1.619	−2.101
13.89	0.072	−3.181	1.794	−2.528	0.345	−3.277	1.994	−2.898	−3.084	1.593	−2.158
10	0.1	−2.802	1.815	−2.671	0.333	−3.549	2.106	−2.671	−2.054	1.524	−2.671
7.19	0.139	−2.893	1.837	−2.581	0.325	−3.633	2.16	−2.681	−2.153	1.513	−2.481
5.18	0.193	−3.089	1.84	−2.454	0.316	−3.736	2.159	−2.63	−2.442	1.521	−2.279
3.73	0.268	−3.173	1.821	−2.42	0.314	−3.735	2.111	−2.615	−2.611	1.531	−2.225
2.68	0.373	−3.245	1.796	−2.389	0.31	−3.775	2.055	−2.556	−2.715	1.536	−2.221
1.93	0.518	−3.239	1.782	−2.427	0.311	−3.762	2.028	−2.585	−2.715	1.536	−2.269
1.39	0.72	−3.23	1.777	−2.455	0.311	−3.741	2.017	−2.623	−2.718	1.536	−2.287
1	1	−3.231	1.774	−2.462	0.312	−3.745	2.011	−2.622	−2.717	1.537	−2.303

Table 10 Coefficients for SVV in cm/s, with Φ_{j1} for INS and Φ_{j2} for G.MUC (INS, POI and simulations for MUC) and $j = 1, 2, 3$

f (Hz)	T (s)	β_1	β_2	β_3	σ	Φ_{11}	Φ_{21}	Φ_{31}	Φ_{12}	Φ_{22}	Φ_{32}
100	0.01	−3.122	0.719	−1.861	0.508	−3.122	1.339	−3.379	−3.122	0.099	−0.343
71.43	0.014	−2.563	0.771	−2.205	0.528	−2.563	1.493	−3.865	−2.563	0.049	−0.545
52.63	0.019	−2.613	1.029	−2.374	0.517	−2.613	1.724	−3.875	−2.613	0.335	−0.874
37.04	0.027	−3.046	1.393	−2.398	0.489	−3.046	1.976	−3.572	−3.046	0.809	−1.225
27.03	0.037	−3.448	1.694	−2.377	0.49	−3.448	2.088	−3.115	−3.448	1.3	−1.639
19.23	0.052	−3.504	2.03	−2.854	0.5	−3.504	2.078	−2.854	−3.504	1.981	−2.854
13.89	0.072	−3.526	1.945	−2.584	0.485	−3.526	1.996	−2.584	−3.526	1.894	−2.584
10	0.1	−3.746	1.905	−2.312	0.464	−3.746	1.959	−2.312	−3.746	1.85	−2.312
7.19	0.139	−3.99	1.932	−2.192	0.445	−3.99	1.976	−2.192	−3.99	1.889	−2.192
5.18	0.193	−4.094	1.947	−2.208	0.436	−4.032	1.947	−2.208	−4.156	1.947	−2.208
3.73	0.268	−3.95	1.861	−2.226	0.43	−3.95	1.861	−2.226	−3.95	1.861	−2.226
2.68	0.373	−3.864	1.828	−2.304	0.436	−3.864	1.828	−2.304	−3.864	1.828	−2.304
1.93	0.518	−3.814	1.815	−2.36	0.437	−3.814	1.815	−2.36	−3.814	1.815	−2.36
1.39	0.72	−3.816	1.829	−2.398	0.438	−3.816	1.829	−2.398	−3.816	1.829	−2.398
1	1	−3.821	1.831	−2.404	0.442	−3.821	1.831	−2.404	−3.821	1.831	−2.404

The chosen structure is a low-rise residential building described in Fig. 26 and Table 11. We assume it is situated in the G.MUC region; therefore, we adopted the site-specific GMPE for SVH and SVV from Tables 9 and 10 respectively, for G.MUC and random effects with coefficients $\Phi_{12}, \Phi_{22}, \Phi_{32}$. We assume a 5% modal damping ratio for all the modes. After estimating the spectral velocities, maximum velocities at the ceilings, in
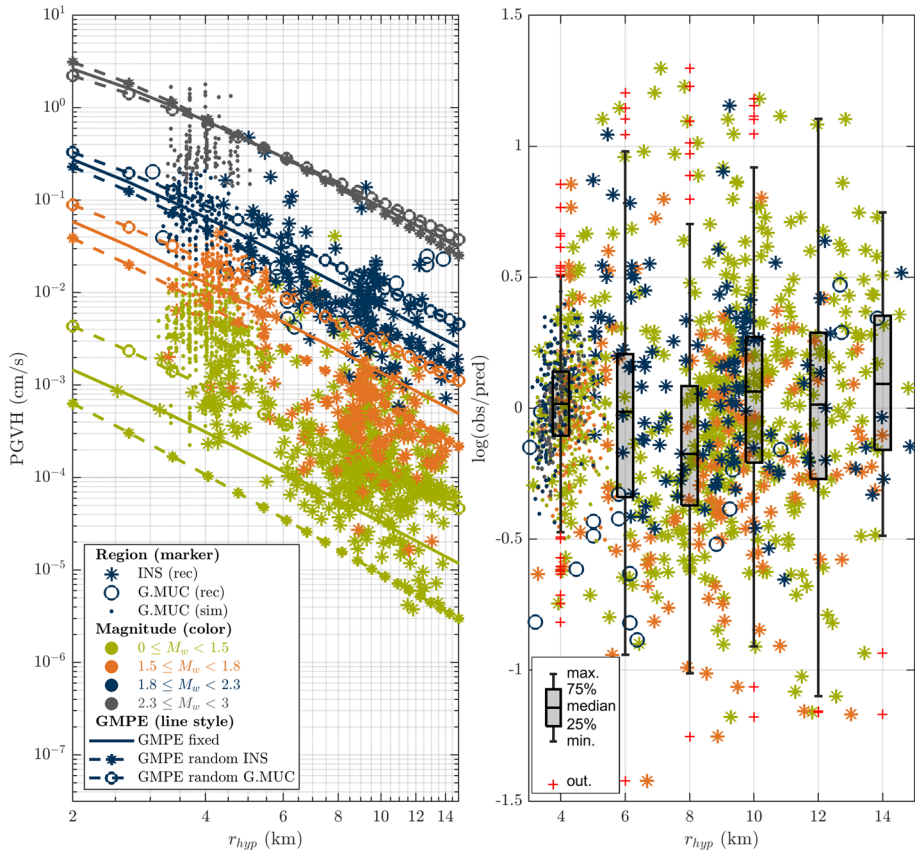
Fig. 20 Regression curves for PGVH in cm/s: left) GMPE with fixed and random effects for different magnitude bins (in different colors) compared to the recorded and simulated data; right) residuals of the GMPE (pred.) with respect to the recorded and simulated data (obs.)

horizontal and vertical directions, are obtained through a multi-modal response spectrum analysis following the DIN 4149 standard (DIN 2005). Alternatively, one can use the national annex of the Eurocode 8 (DIN 2023), which additionally includes new earthquake maps for Germany in the form of spectral response accelerations and new subsoil maps. This does not have an influence here, as the spectral quantities are derived from the proposed GMPE, not from the standard codes.

A finite element model (FEM) is utilized to extract natural frequencies, mode shapes, effective modal mass and cumulative mass fraction (CMF) as listed in Table 12 and shown in Figs. 27 and 28. The modal superposition for the horizontal directions is performed via SRSS. In vertical direction, the activated modes are closely spaced, therefore we apply a complete quadratic combination method (CQCM) according to Wilson et al. (1981).

The assessment of the building response based on limit values for serviceability is performed according to the DIN 4150-3 (DIN 2016), for short-term excitations, where the limit values are designed to prevent permanent effects that would reduce the utility value of the affected building or component with respect to its intended use. The standard code differentiates between short-term vibrations, which are vibrations that occur infrequently enough to prevent material fatigue and whose timing and duration are insufficient to cause
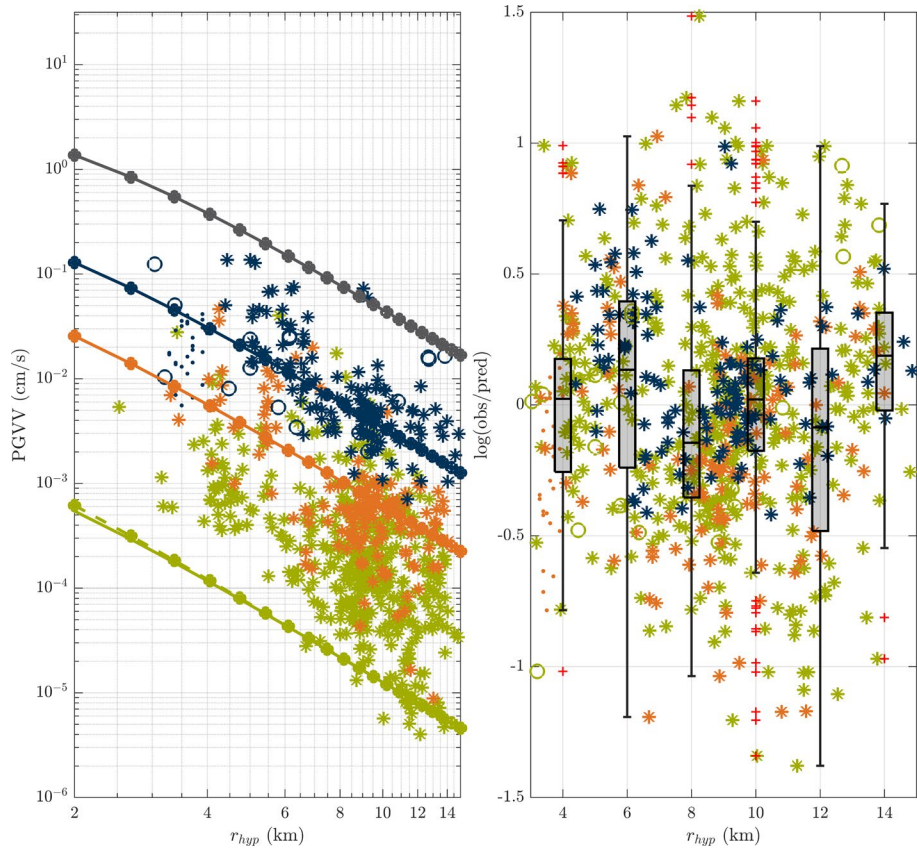
Fig. 21 Regression curves for PGVV in cm/s: left) GMPE with fixed and random effects for different magnitude bins (in different colors) compared to the recorded and simulated data; right) residuals of the GMPE (pred.) with respect to the recorded and simulated data (obs.). Legend same as in Fig. 20

significant resonance amplification in the affected structure, and continuous vibrations. Micro-earthquakes belong to the first category, being a transient vibration.

In horizontal direction, the verification relies on horizontal vibration velocities at the top ceiling level, considering the maximum of the two horizontal components (x, y). Alternatively, the assessments can be made at the building's foundation, using the largest value of the three velocity components (x, y, z). Limit values for these components are provided in Table 13 for different building types, in dependency of the as a function of the most relevant frequency range. This is the frequency range corresponding to the largest velocities in frequency domain. As shown in a previous study (Taddei et al. 2022), the frequency range of interest is different for the vertical and the horizontal direction and needs to be chosen carefully, when using PGVH and PGVV values for the verification.

In the vertical direction, looking at the ceiling oscillations, a reduction in the serviceability of the ceiling is not expected if $v_{z,max} \leq 20$ mm/s at the location of the highest vibration speed, typically in the center of the ceiling (refer to Table 13, last column from right).
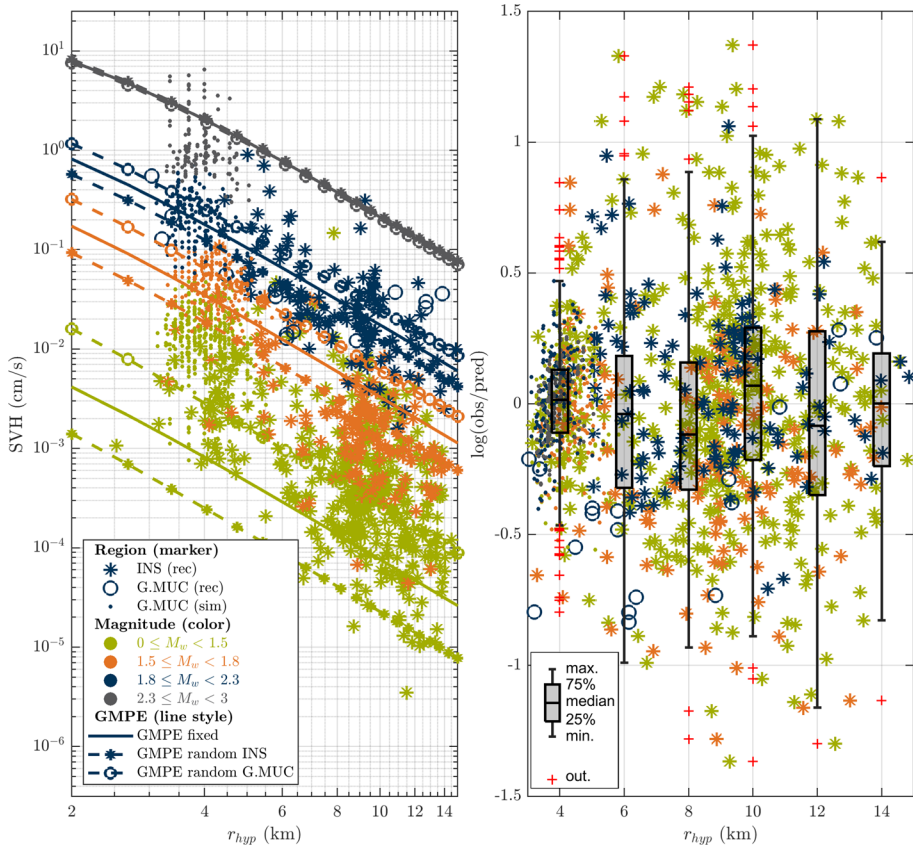
Fig. 22 Regression curves for SVH in cm/s at $T = 0.1$ s: left) GMPE with fixed and random effects for different magnitude bins (in different colors) compared to the recorded and simulated data; right) residuals of the GMPE (pred.) with respect to the recorded and simulated data (obs.)

Here, we focus on residential buildings (building type 2 in Table 13). For buildings with special vibration sensitivity (type 3, e.g. monumental buildings), a significant reduction of this reference value may be necessary to prevent minor damages.

The maximum velocities at the highest floor, obtained through modal superposition, are detailed in Table 14 and shown in Fig. 29. For the considered focal depth (D) and epicentral distance (r_{epi}), the serviceability verification is satisfied for a seismic event with a magnitude (M_W) of at least up to 2.5. However, as the earthquake magnitude increases to 3, the verification for serviceability fails. This application highlights the potential application of the proposed GMPE in conducting a more comprehensive risk assessment. For example, the GMPEs can be integrated into a Monte Carlo analysis which includes also the prediction uncertainties of the regression curves as well as the building variability. This would offer a deeper understanding of the potential impact of seismic events on structural integrity and aiding in the development of robust risk mitigation strategies, especially for EGS.
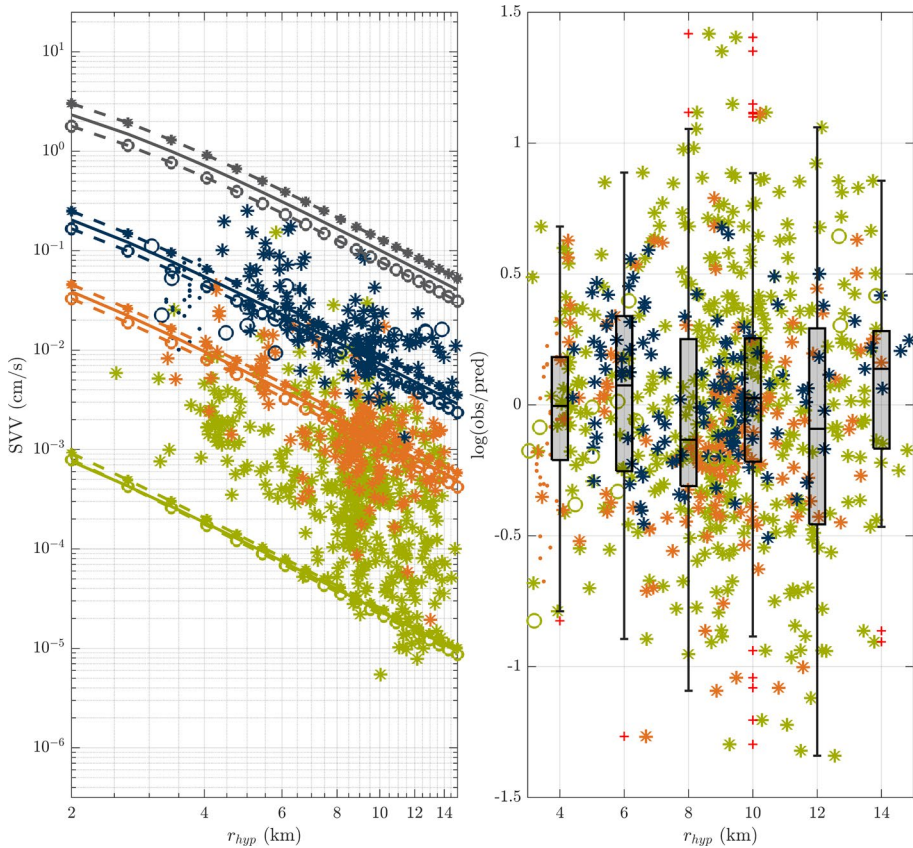
Fig. 23 Regression curves for SVV in cm/s at $T = 0.1$ s: left) GMPE with fixed and random effects for different magnitude bins (in different colors) compared to the recorded and simulated data; right) residuals of the GMPE (pred.) with respect to the recorded and simulated data (obs.). Legend same as in Fig. 22

6 Conclusion and outlook

Geothermal energy provides a clean and renewable power source but is associated with induced seismicity risks in certain regions, requiring careful monitoring and mitigation measures.

Our study begins with a statistical analysis of recorded seismic data from the GPP in Insheim and expands to include data from the Munich region. We incorporate scarce Munich data with physics-based simulations to generate ground motion models expressed in response spectra. This comprehensive approach combines recorded and simulated data, offering valuable insights into ground motion characteristics.

Comparisons of three considered GMPEs with data reveal disparities, especially at shorter periods. While the KHS model aligns better with data for periods below 0.1 s, it lacks accuracy for larger periods. The ATK and DGL models closely track each other but consistently provide lower values than observed, potentially due to the different magnitude and distance ranges, different assumptions about soil conditions and to systematic differences in the calculation procedures of seismic magnitude, such as variations in the utilization of local magnitude among different databases, or variations in the conversion process from M_L to M_W.
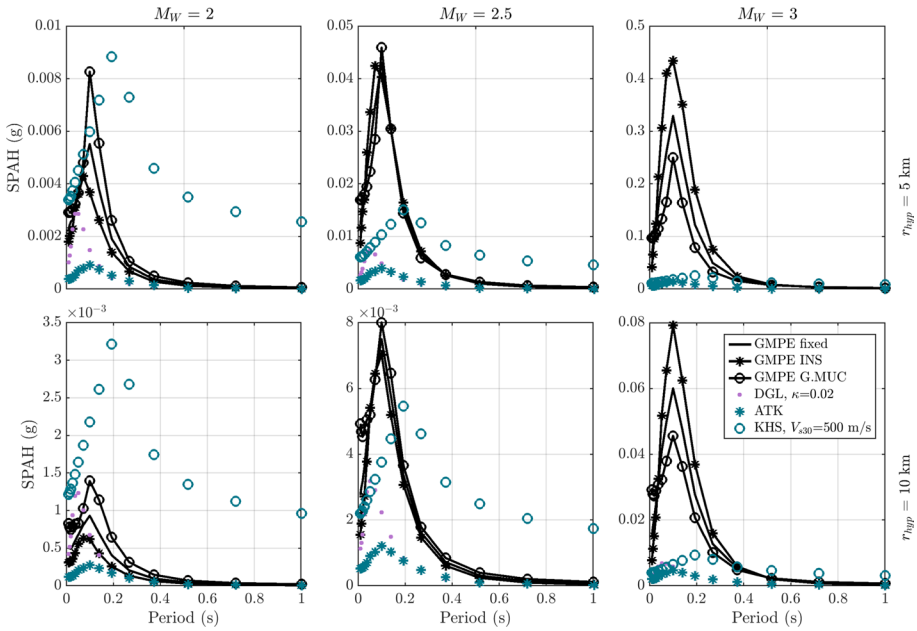
Fig. 24 Comparison of the proposed GMPE for SPAH in g and existing models across various magnitudes and distances, using a linear scale for clarity
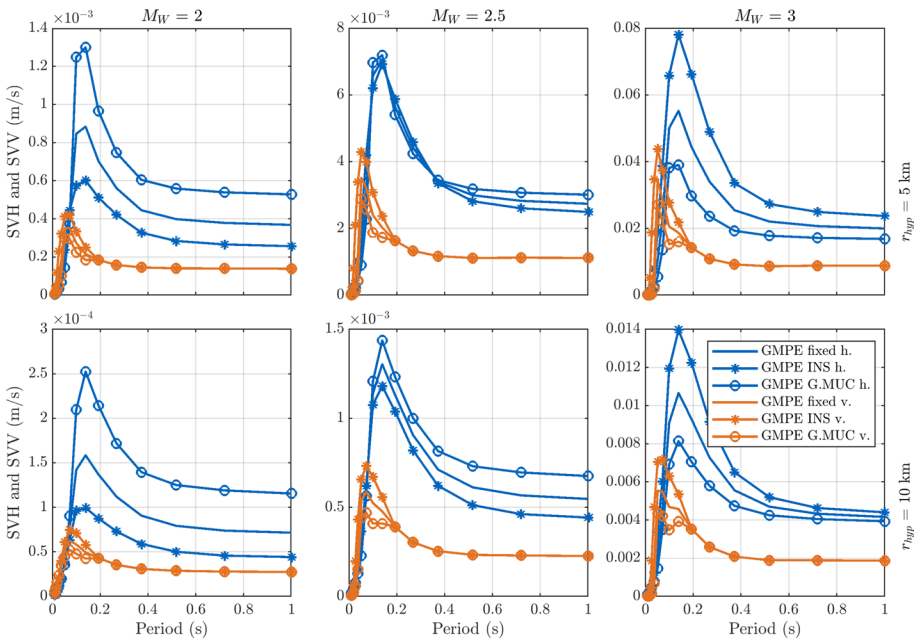

Fig. 25 Proposed GMPE for SVH and SVV in m/s across various magnitude and distance bins. In the legend $h.$ stands for horizontal and $v.$ for vertical

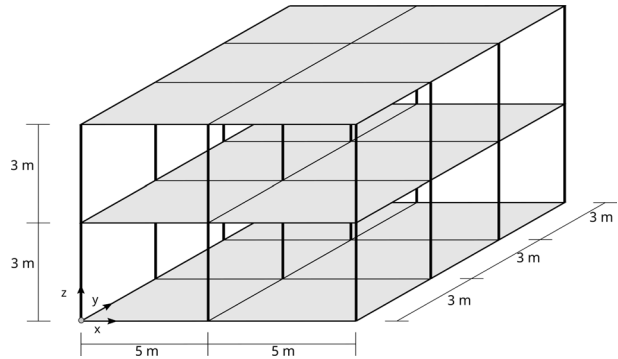**Fig. 26** Sketch of the frame structure used in the example

Table 11 Building and foundation parameters

Parameter	Value
Elastic modulus	30,000 MPa
Density	2500 kg/m^3
Poisson's ratio	0.27
Damping ratio	0.05
Floor thickness	0.2 m
Column length	3 m
Column cross-section	0.3 m × 0.3 m
Beam cross-section	0.3 m × 0.3 m

Table 12 Natural properties and mode types of the considered building

Dir.	Nr.	f_i (Hz)	T_i (s)	Mode type	$M_{i,eff}$ (kg)	CMF (%)
x	1	2.586	0.39	Global, 1. Bending	183491.0	91
	2	7.705	0.129	Global, 2. Bending	17689.9	99
y	1	2.604	0.38	Global, 1. Bending	183491.0	91
	2	7.735	0.129	Global, 2. Bending	17689.9	99
z	1	14.66	0.068	Local bending mode, 2nd floor, external wings	25996.7	15
	2	15.68	0.064	Local bending mode, 2nd floor, central wing	125,314	87
	3	18.23	0.055	Local bending mode, 1st floor, central wing	15950.6	96

We propose a hybrid functional form, combining features from KHS and ATK models, emphasizing the need for adapting GMPEs to regional and project-specific characteristics and addressing the challenge of higher spectral quantities at shorter periods, crucial for accurate predictions in the studied region. We propose regression coefficients for spectral accelerations and velocities, separating the horizontal and the vertical directions. As the project advances and further data become available from the local seismic monitoring networks, installed as part of the project, these coefficients can be reevaluated. The reevaluation should be conducted after the occurrence of at least five more earthquakes with a moment magnitude (M_W) greater than 1.5.

Applying spectral velocities derived from our models, we evaluate a low-rise residential building's response for the G.MUC region. Using multi-modal response spectrum analysis, we assess the building's serviceability against current German standards. The proposed
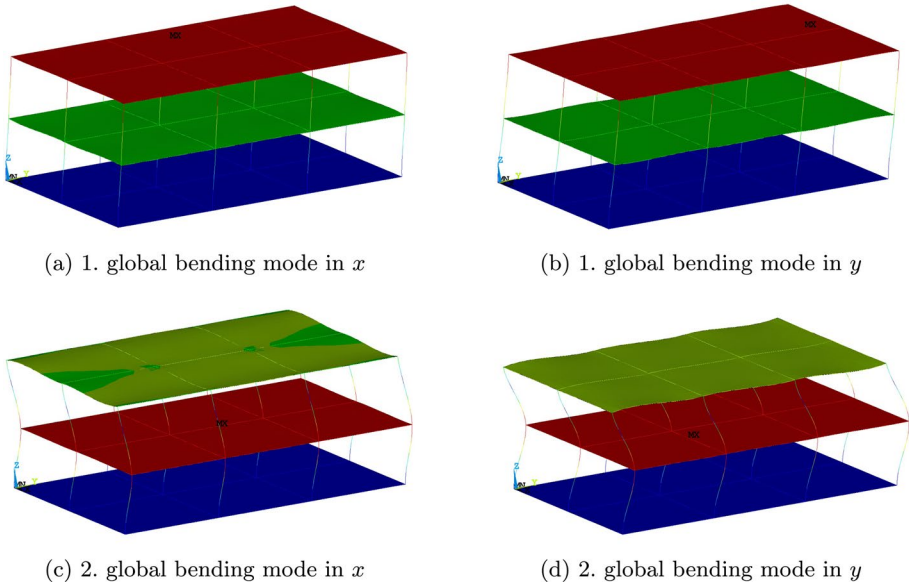
(a) 1. global bending mode in x

(b) 1. global bending mode in y

(c) 2. global bending mode in x

(d) 2. global bending mode in y

Fig. 27 Illustration of the contributing modes in x and y direction. The color bar is not given as the exact relative deformation values in the mode shapes are not important; only the shape itself is significant. Red indicates the maximum relative deformation, and blue indicates the minimum

(a) Local bending mode, 2nd floor, external wings.

(b) Local bending mode, 2nd floor, central wing.

(c) Local bending mode, 1st floor, central wing.

Fig. 28 Illustration of the contributing modes in z direction. The color bar is not given as the exact relative deformation values in the mode shapes are not important; only the shape itself is significant. Red indicates the maximum relative deformation, and blue indicates the minimum
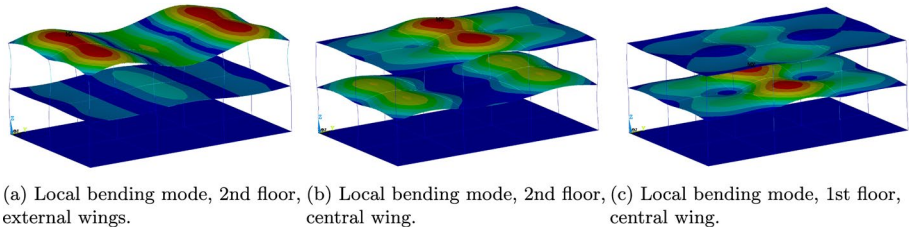

(a) Horizontal response in terms of max. velocities (scale fact. 100).

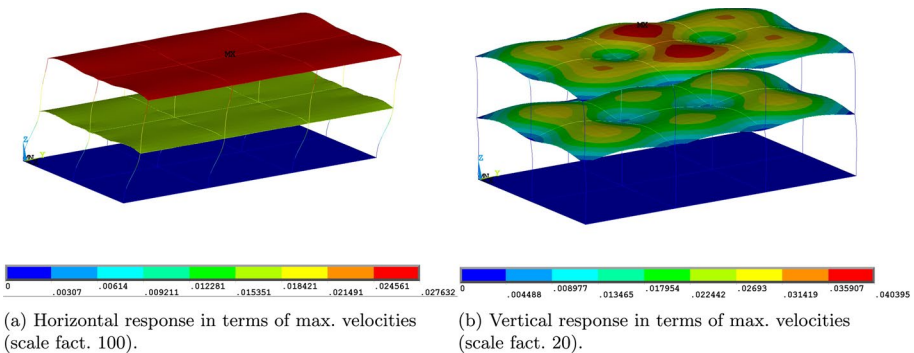(b) Vertical response in terms of max. velocities (scale fact. 20).

Fig. 29 Illustration of the velocity distribution after modal superposition in horizontal and vertical direction, for $M_W = 3$. The units of the color bar are m/s

Table 13 Reference values $v_{i,\max}$ for assessing the effect of short-term vibrations on buildings. (DIN 2016)

Type of building	Limit values for $v_{i,\max}$ in mm/s				
	Foundation, all dir., $i = x,y,z$			Highest floor, hor., $i = x,y$	Ceilings vert., $i = z$
	Frequencies			all freq.	all freq.
	1 -10 Hz	10-50 Hz	50-100 Hz		
1 Commercially-used and industrial buildings	20	20 to 40	40 to 50	40	20
2 Residential buildings and similar structure (for their construction type and/or use)	5	5 to 15	15 to 20	15	20
3 Buildings with special vibration sensitivity that do not conform to those in rows 1 and 2, and are particularly valuable (e.g., under monument protection)	3	3 to 8	8 to 10	8	20

Table 14 Maximum velocities at the highest floor for different M_W and for $D = 4$ km and $r_{epi} = 3$ km, compared to the reference values $v_{i,max}$ for assessing the effect of short-term vibrations on buildings (building type 2)

	max (v_i) (mm/s)	M_W			Thresholds (mm/s)
		2	2.5	3	
Horizontal	x, y	**0.88**	**5.0**	*27.6*	<15
Vertical	z	**0.47**	**4.4**	*40.4*	<20

Bold indicates maximum velocities smaller than the threshold, italic larger than the threshold in Table 13

models provide insights into ceiling oscillations, indicating a need for careful consideration of frequency ranges. The study establishes a foundation for more extensive risk assessment, including building variability within a Monte Carlo analysis, underlining the importance of regional calibration for accurate predictions.

Appendix A: List of acronyms

See Table 15.

Table 15 List of acronyms, in order of appearance

GPP	Geothermal power plan
EGS	Enhanced geothermal system
GMM	Ground motion model
GMPE	Ground motion prediction equation
GI	Geothermal Induced
GAB	Geothermie Allianz Bayern
URG	Upper Rhine Graben
ANOVA	ANalysis of variance
BMA	Bayesian model averaging
PGAH	Peak ground acceleration in horizontal direction in g or m/s^2 or cm/s^2
PGAV	Peak ground acceleration in vertical direction in g or m/s^2 or cm/s^2
PGVH	Peak ground velocity in horizontal direction in m/s or cm/s
PGVV	Peak ground velocity in vertical direction in m/s or cm/s
SPAH	Spectral pseudo acceleration in horizontal direction in g or m/s^2 or cm/s^2
SPAV	Spectral pseudo acceleration in vertical direction in g or m/s^2 or cm/s^2
SPVH	Spectral pseudo velocity in horizontal direction in m/s or cm/s
SPVV	Spectral pseudo velocity in vertical direction in m/s or cm/s
SVH	Spectral Velocity in Horizontal direction in m/s or cm/s
SVV	Spectral velocity in vertical direction in m/s or cm/s
LME	Linear mixed-effects
FEM	Finite element model
SRSS	Square root of the sum of the squares
CQCM	Complete quadratic combination method
CMF	Cumulative mass fraction

Appendix B: Stations-events matrices

Table 16 List of selected events for the Insheim area in the 1st period

Nr.	Origin time	M_L	Lat.	Long.	Depth [km]
–	2009-05-08T19:23:18	2.1	49.150	8.160	3
–	2009-05-08T20:33:09	2.0	49.150	8.150	3
–	2009-05-08T22:28:32	2.0	49.160	8.150	3
1	2009-10-18T19:12:12	1.5	49.148	8.164	5
2	2010-04-07T09:04:04	1.6	49.140	8.160	5
3	2010-04-07T13:46:21	1.7	49.140	8.160	5
-	2010-04-09T10:52:22	2.4	49.150	8.151	5
4	2010-04-09T12:36:33	2.2	49.148	8.157	5
5	2012-11-12T11:15:04	1.8	49.143	8.160	5
6	2012-11-12T12:53:02	1.5	49.141	8.157	5
7	2013-01-26T19:48:27	1.8	49.159	8.153	5
8	2013-02-17T20:07:15	2.0	49.161	8.152	4
9	2013-10-02T01:13:26	2.1	49.162	8.152	4
10	2013-11-18T12:54:15	1.5	49.144	8.146	6
11	2013-11-21T14:15:22	1.9	49.150	8.154	5
12	2016-02-12T06:26:04	1.7	49.146	8.150	5
13	2016-07-14T17:49:10	1.9	49.150	8.156	5

Table 17 Matrix of the stations which recorded the events in the first period

Station-event	1	2	3	4	5	6	7	8	9	10	11	12	13
INS1							x	x	x	x	x	x	
INS2					x	x	x	x	x	x	x		
INS3					x	x	x	x	x	x	x	x	x
INS4					x	x	x	x	x	x	x		
INS4B												x	x
INS5					x	x	x	x	x	x	x	x	x
INS6					x	x	x	x	x	x	x		
INS6B												x	x
INS7							x	x	x	x	x	x	x
INS8												x	x
INS9													
INSH					x	x	x	x	x	x	x	x	x
LDAU	x	x	x	(x)									
TMO20									x	x	x	x	x
TMO22									x	x	x		x
TMO54									x	x	x	x	x
TMO55									x	x	x	x	x
TMO57												x	x
TMO66												x	x
A127A												x	

Each cross represents a set of 3 recordings in the 3 directions (*Z, N, E*). The cross between brackets indicates a discarded set of recordings

Table 18 List of selected events for the Insheim area in the 2nd period

Nr.	Origin time	M_L	Lat.	Long.	Depth [km]
1	2023-01-11T13:55:29	0.7	8.168	49.174	5
2	2023-01-10T19:02:01	0.7	8.134	49.144	7.9
3	2023-01-10T10:45:58	2	8.15	49.157	8.9
4	2022-12-22T06:05:04	1.7	8.155	49.147	5
5	2022-12-17T07:24:35	1.9	8.155	49.155	5
6	2022-11-28T17:38:35	0.5	8.147	49.169	7
7	2022-11-19T03:59:04	0.8	8.171	49.157	6.1
8	2022-09-22T02:36:06	0.5	8.144	49.164	3.8
9	2022-09-20T20:45:41	0.7	8.143	49.162	6
10	2022-07-21T23:47:40	0.6	8.141	49.153	5
11	2022-04-27T22:54:46	0.5	8.158	49.154	4
12	2022-04-25T00:58:55	0.5	8.16	49.145	3.7
13	2022-03-16T14:53:57	1	8.147	49.149	3
14	2022-03-16T01:11:52	0.3	8.144	49.153	3.8
15	2022-03-07T03:05:03	0.7	8.15	49.155	3.1
16	2022-03-01T22:39:16	0.4	8.155	49.147	4
17	2022-02-28T19:32:17	0.6	8.139	49.145	3.8
18	2022-02-01T00:48:12	1.2	8.147	49.149	5.2
19	2022-01-31T04:06:10	1.2	8.147	49.15	5.2
20	2022-01-25T15:27:49	1.1	8.147	49.132	5
21	2022-01-11T22:36:30	0.4	8.188	49.149	4
22	2022-01-08T07:28:29	0.6	8.135	49.154	4
23	2021-12-30T18:31:50	0.8	8.162	49.159	3.7
24	2021-12-23T13:54:18	0.8	8.176	49.155	4
25	2021-12-22T01:21:05	0.3	8.189	49.171	4
26	2021-12-15T23:02:26	0.3	8.17	49.169	4
27	2021-12-15T18:17:05	0.3	8.152	49.156	4
28	2021-12-13T21:01:08	0.6	8.147	49.139	5.2
29	2021-12-11T04:13:21	0.6	8.147	49.148	4
30	2021-12-06T16:50:11	0.9	8.155	49.151	4
31	2021-11-25T02:12:54	0.2	8.149	49.146	2.9
32	2021-11-25T00:08:56	0.4	8.155	49.15	4
33	2021-11-19T22:51:54	0.5	8.149	49.148	4
34	2021-11-18T06:58:45	0.5	8.155	49.147	2.4
35	2021-11-03T20:40:15	0.9	8.147	49.15	3.9
36	2021-09-30T23:15:16	0.5	8.156	49.153	4
37	2021-08-21T17:00:29	1.2	8.146	49.149	4
38	2021-08-21T16:25:38	1.1	8.146	49.149	4
39	2021-08-18T06:18:09	1.2	8.164	49.185	4
40	2021-08-05T23:33:26	0.4	8.22	49.184	4
41	2021-07-30T19:46:16	0.7	8.148	49.153	5.2
42	2021-06-28T22:30:14	0.2	8.186	49.149	4
43	2021-06-07T23:00:44	0	8.175	49.158	4
44	2021-06-06T00:58:34	0.4	8.157	49.149	4
45	2021-06-05T21:55:22	1	8.155	49.153	3.9
46	2021-06-04T11:23:23	0.8	8.155	49.157	4

Table 18 (continued)

Nr.	Origin time	M_L	Lat.	Long.	Depth [km]
47	2021-06-01T17:45:54	0.5	8.168	49.148	4
48	2021-06-01T07:17:40	0.6	8.152	49.145	4
49	2021-04-29T01:38:05	0.3	8.147	49.162	6.3
50	2021-04-21T04:22:48	0.3	8.141	49.157	4
51	2021-03-27T14:18:43	1.3	8.141	49.158	5
52	2021-03-16T21:54:23	0.4	8.142	49.154	3.9
53	2021-02-26T16:28:45	1.2	8.161	49.163	5.3
54	2021-01-08T05:14:16	0.7	8.15	49.14	7.7
55	2020-11-09T21:47:07	1.1	8.135	49.154	7

The corresponding event-station matrix is availbale as an excel file in data and resources

Table 19 Stations-events matrix for Poing and Unterhaching

Station-Event	POI						UH	
	1	2	3	4	5	6	7	8
BHF1S					x			
HIS8S			x					
HWMRS						x		
LP01S	x	x	x		x	x		
MS1						x		
POI01					x			
POI02					x			
POI03					x			
Poing					x	x		
RHS26						x		
SCH6S						x		
SIS21			x			x		
WS15S	x		x	x	x	x		
UH1							x	x
UH2							x	x
UH3							x	x
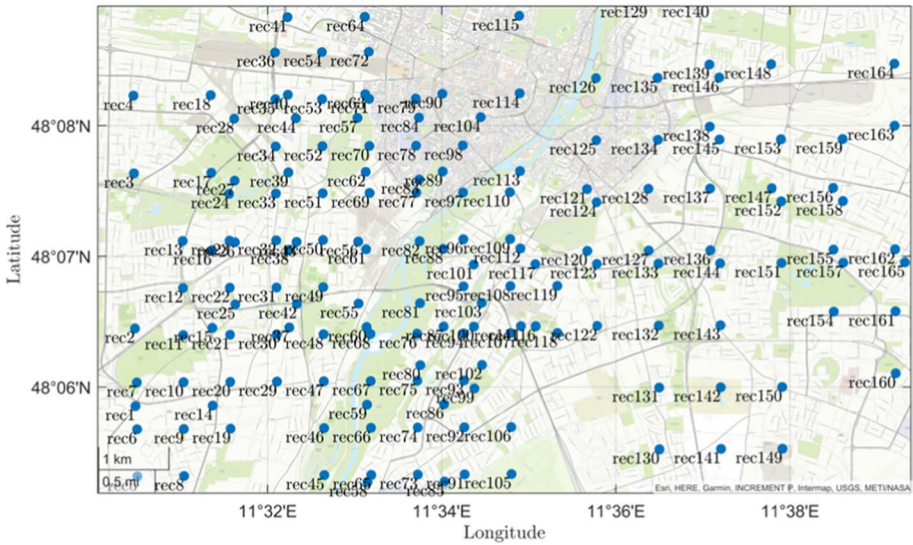
Fig. 30 Distribution of stations for the simulations of the Munich scenarios. Not all the stations recorded all the 23 events. This selection was based on the station distance from the epicenter and the magnitude of the events, ensuring that the quality of the simulated signals was high enough for reliable analysis

Appendix C: Regression plots for peak ground accelerations

See Figs. 31 and 32.
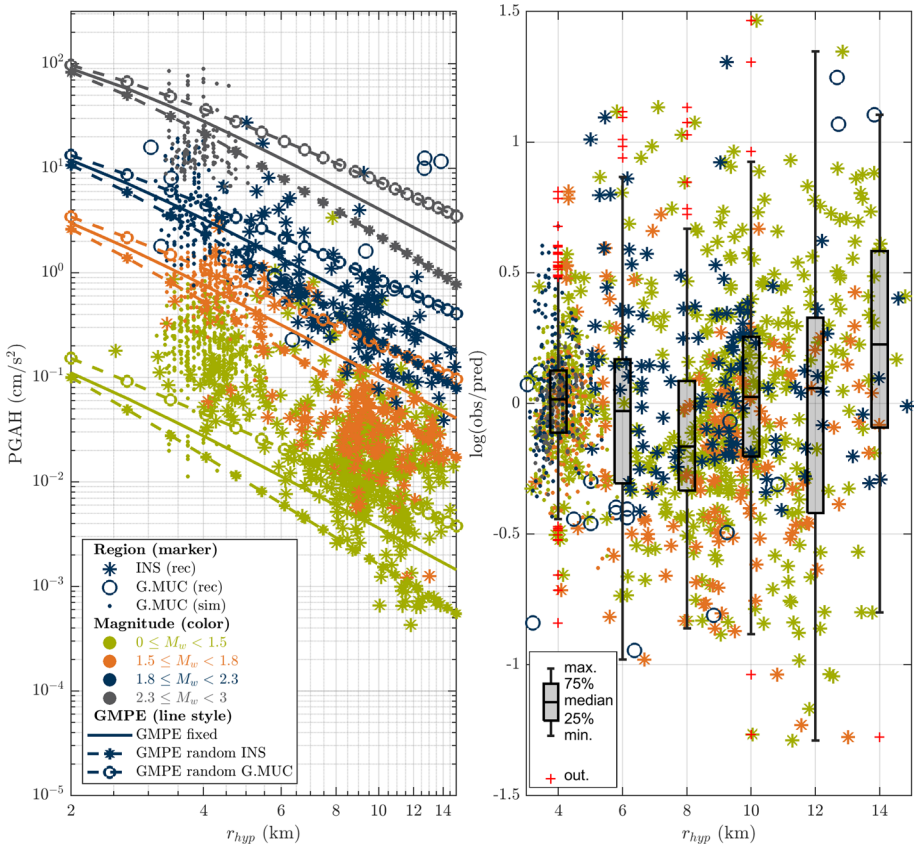
Fig. 31 Regression curves for PGAH in cm/s^2: left) GMPE with fixed and random effects for different magnitude bins (in different colors) compared to the recorded and simulated data; right) residuals of the GMPE (pred.) with respect to the recorded and simulated data (obs.)
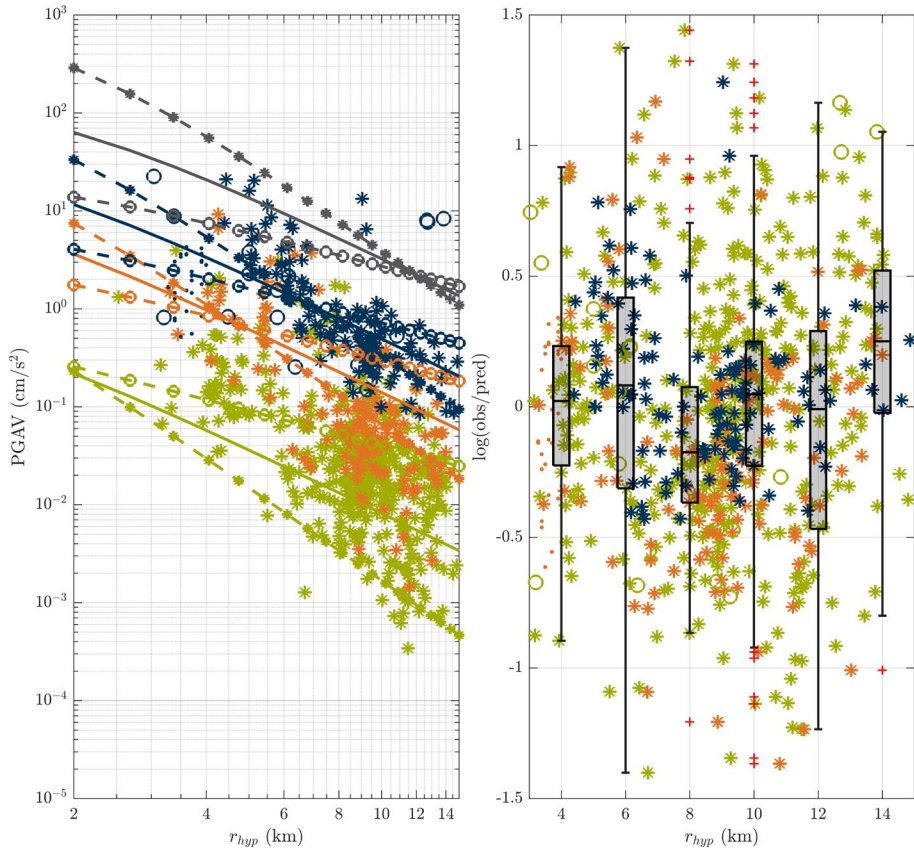
Fig. 32 Regression curves for PGAV in cm/s²: left) GMPE with fixed and random effects for different magnitude bins (in different colors) compared to the recorded and simulated data; right) residuals of the GMPE (pred.) with respect to the recorded and simulated data (obs.). Legend same as in Fig. 31

Data and resources The event-station matrix for Insheim, for the second period, is available in form of a digital file. A Matlab function for the proposed GMPE with respect to M_W and M_L is accessible at: https://github.com/ChairOfStructuralMechanicsTUM/GMPE_induced_DE.

Declarations

Conflict of interest The authors declare no Conflict of interest regarding the presented study.

Ethical approval No ethical approval was required for this study as it exclusively utilized information freely available in the public domain and did not involve animals or human subjects. Additionally, the research was authorized through the Bavarian State Ministry for Science and Art.

Informed consent Informed consent was obtained from all participants involved in data collection and analysis.

References

Abrahamson NA, Youngs RR (1992) A stable algorithm for regression analyses using the random effects model. Bull Seismol Soc Am 82(1):505–510

Afanasiev M, Boehm C, Driel M, Krischer L, Rietmann M, May DA, Knepley MG, Fichtner A (2019) Modular and flexible spectral-element waveform modelling in two and three dimensions. Geophys J Int 216(3):1675–1692

Allmann B, Edwards B, Bethmann F, Deichmann N (2010) Appendix I Determination of MW and calibration of ML (SED)-MW regression

Atkinson GM (2006) Single-station sigma. Bull Seismol Soc Am 96(2):446–455

Atkinson GM (2015) Ground-motion prediction equation for small-to-moderate events at short hypocentral distances, with application to induced-seismicity hazards. Bull Seismol Soc Am 105(2A):981–992

Atkinson GM, Assatourians K (2017) Are ground-motion models derived from natural events applicable to the estimation of expected motions for induced earthquakes? Seismol Res Lett 88(2A):430–441

Beichel K, Koch R, Wolfgramm M (2014) Die Analyse von Spülproben zur Lokalisierung von Zuflusszonen in Geothermiebohrungen. Beispiel der Bohrungen Gt Unterhaching 1/1a und 2.(Süddeutschland, Molassebecken, Malm). Geologische Blätter für Nordost–Bayern 64(1–4):43–65

BGR (2023) Federal Institute for Geosciences and Natural Resources, Seismizität in Deutschland. https://www.bgr.bund.de/MAGS/DE/Hintergrundinformation/Seismizitaet/seismizitaet_node.html. 14 Oct 2023

BGR (2023) Microseismic Activity of Geothermal Systems (MAGS). https://www.mags-projekt.de/MAGS/DE/Home/MAGS_node.html. 14 Oct 2023

BGR (2023) Seismic monitoring of deep geothermal plants and possible seismic impacts (SEIGER). https://www.bgr.bund.de/DE/Themen/Erdbeben-Gefaehrdungsanalysen/Ingenieurseismologische_Gefaehrdungsanalysen/SEIGER/DE/Downloads/downloads_node.html. 14 Oct 2023

Bommer JJ, Dost B, Edwards B, Stafford PJ, Elk J, Doornhof D, Ntinalexis M (2016) Developing an application-specific ground-motion model for induced seismicity. Bull Seismol Soc Am 106(1):158–173

Bommer JJ, Stafford PJ, Ruigrok E, Rodriguez-Marek A, Ntinalexis M, Kruiver PP, Edwards B, Dost B, Elk J (2022) Ground-motion prediction models for induced earthquakes in the Groningen gas field, the Netherlands. J Seismolog 26(6):1157–1184

Boore DM, Youngs RR, Kottke AR, Bommer JJ, Darragh R, Silva WJ, Stafford PJ, Al Atik L, Rodriguez-Marek A, Kaklamanos J (2022) Construction of a ground-motion logic tree through host-to-target region adjustments applied to an adaptable ground-motion prediction model. Bull Seismol Soc Am 112(6):3063–3080

Buijze L, Bijsterveldt L, Cremer H, Paap B, Veldkamp H, Wassing BB, Van Wees J-D, Yperen GC, Heege JH, Jaarsma B (2019) Review of induced seismicity in geothermal systems worldwide and implications for geothermal systems in the netherlands. Neth J Geosci 98:13

Cremen G, Werner MJ, Baptie B (2020) A new procedure for evaluating ground-motion models, with application to hydraulic-fracture-induced seismicity in the United Kingdom. Bull Seismol Soc Am 110(5):2380–2397

Dalmais E, Ravier G, Maurer V, Fries D, Genter A, Pandélis B (2022) Environmental and Socio-Economic Impact of Deep Geothermal Energy, an Upper Rhine Graben Perspective. IntechOpen, London

DIN (2005) DIN 4149, Buildings in German seismic zones—Load assumptions, design and construction of common building structures; Issue date: 2005-04. German version

DIN (2016) DIN 4150. 2016-12. DIN 4150-3: structural vibrations—Part 3: effects of vibration on structures. German Standards Organization (GSO) Berlin

DIN (2023) DIN EN 1998-1/NA:2023-11: National Annex—Nationally determined parameters—Eurocode 8: Design of structures for earthquake resistance—Part 1: General rules, seismic actions and rules for buildings. German Standards Organization (GSO) Berlin

Dost B, Ruigrok E, Spetzler J (2017) Development of seismicity and probabilistic hazard assessment for the Groningen gas field. Neth J Geosci 96(5):235–245

Douglas J (2004) Use of analysis of variance for the investigation of regional dependence of strong ground motions. In: Proc. of the Thirteenth World conf. equation engineering

Douglas J, Edwards B, Convertito V, Sharma N, Tramelli A, Kraaijpoel D, Cabrera BM, Maercklin N, Troise C (2013) Predicting ground motion from induced earthquakes in geothermal areas. Bull Seismol Soc Am 103(3):1875–1897

Edwards B, Douglas J (2013) Selecting ground-motion models developed for induced seismicity in geothermal areas. Geophys J Int 195(2):1314–1322

Edwards B, Allmann B, Fäh D, Clinton J (2010) Automatic computation of moment magnitudes for small earthquakes and the scaling of local to moment magnitude. Geophys J Int 183(1):407–420

Groos JC, Fritschen R, Ritter JRR (2013) Untersuchung induzierter Erdbeben hinsichtlich ihrer Spürbarkeit und eventueller Schadenswirkung anhand der DIN 4150. Bauingenieur 88(11)

Grünthal G (2014) Induced seismicity related to geothermal projects versus natural tectonic earthquakes and other types of induced seismic events in Central Europe. Geothermics 52:22–35

Halbert S (2023) IRIS SEED Channel Naming

Keil S, Wassermann J, Megies T (2022) Estimation of ground motion due to induced seismicity at a geothermal power plant near Munich, Germany, using numerical simulations. Geothermics 106:102577

Khansefid A, Bakhshi A, Ansari A (2019) Development of declustered processed earthquake accelerogram database for the Iranian Plateau: including near-field record categorization. J Seismolog 23(4):869–888

Khansefid A, Yadollahi SM, Müller G, Taddei F, Kumawat A (2022) Seismic performance assessment of a masonry building under earthquakes induced by geothermal power plants operation. J Build Eng 48:103909

Khansefid A, Yadollahi SM, Müller G, Taddei F (2022) Induced earthquake hazard by geothermal power plants: statistical evaluation and probabilistic modeling. Int J Disaster Risk Sci 13(5):758–777

Khansefid A, Yadollahi SM, Müller G, Taddei F (2023) Ground motion models for the induced earthquakes by the geothermal power plants activity. J Earthq Eng 27(5):1324–1353

Küperkoch L, Olbert K, Meier T (2018) Long-term monitoring of induced seismicity at the Insheim geothermal site, Germany. Bull Seismol Soc Am 108(6):3668–3683

Lanzano G, Luzi L, Cauzzi C, Bienkowski J, Bindi D, Clinton J, Cocco M, D'Amico M, Douglas J, Faenza L (2021) Accessing European strong-motion data: an update on ORFEUS coordinated services. Seismol Soc Am 92(3):1642–1658

Novakovic M, Atkinson GM, Assatourians K (2018) Empirically calibrated ground-motion prediction equation for Oklahoma. Bull Seismol Soc Am 108(5A):2444–2461

Ntritsos N, Cubrinovski M, Bradley BA (2021) Challenges in the definition of input motions for forensic ground-response analysis in the near-source region. Earthq Spectra 37(4):2562–2595

Prezioso E, Sharma N, Piccialli F, Convertito V (2022) A data-driven artificial neural network model for the prediction of ground motion from induced seismicity: the case of the geysers geothermal field. Front Earth Sci 10:917608

Rodriguez-Marek A, Montalva GA, Cotton F, Bonilla F (2011) Analysis of single-station standard deviation using the KiK-net data. Bull Seismol Soc Am 101(3):1242–1258

Samdaria N, Gupta VK (2018) A new model for spectral velocity ordinates at long periods. Earthq Eng Struct Dyn 47(1):169–194

Schlittenhardt J, Spies T, Kopera J, Morales W (2014) A simple model for probabilistic seismic hazard analysis of induced seismicity associated with deep geothermal systems. Energy Procedia 59:105–112

Schmitt T, Günter L (2014) Ermittlung von momentmagnituden für den deutschen erdbebenkatalog. DACH Mitteilungsblatt, Bauingenieur, in German 89

Schmitt T, G L (2015) Ermittlung von momentmagnituden für den deutschen erdbebenkatalog - ergänzung. DACH Mitteilungsblatt, Bauingenieur, in German 90:90

Sisi AA, Schlittenhardt J, Spies T (2017) Investigation of non-stationarity associated with induced seismicity and its implication in probabilistic seismic hazard analysis. In: AGIS/ESC workshop on induced seismicity and modelling approaches

Steinberg A, Hobiger M, Gaebler P, Vasurya-Bathke H, Sisi AA (2023) Framework for Deterministic Earthquake Ground Motion Maps in Germany using Machine Learning. In: XXVIII general assembly of the international union of geodesy and geophysics (IUGG)

Taddei F, Kumawat A, Csuka A, Cudmani R, Müller G (2022) Input characterisation for low-amplitude seismicity induced by geothermal operations. In: International conference on noise and vibration engineering (ISMA)

Vasterling M, Wegler U, Becker J, Brüstle A, Bischoff M (2017) Real-time envelope cross-correlation detector: application to induced seismicity in the Insheim and Landau deep geothermal reservoirs. J Seismolog 21(1):193–208

Weatherill G, Cotton F (2020) A ground motion logic tree for seismic hazard analysis in the stable cratonic region of Europe: regionalisation, model selection and development of a scaled backbone approach. Bull Earthq Eng 18(14):6119–6148

Wilson EL, Der Kiureghian A, Bayo E (1981) A replacement for the srss method in seismic analysis. Earthq Eng Struct Dyn 9(2):187–192

Wolfgramm M, Bartels J, Hoffmann F, Kittl G, Lenz G, Seibt P, Schulz R, Thomas R, Unger HJ (2007) Unterhaching geothermal well doublet: structural and hydrodynamic reservoir characteristic; Bavaria (Germany). In: European Geothermal Congress, vol. 30

Zalachoris G, Rathje EM (2019) Ground motion model for small-to-moderate earthquakes in Texas, Oklahoma, and Kansas. Earthq Spectra 35(1):1–20

Authors and Affiliations

Francesca Taddei[1] [ORCID] **· Sabrina Keil[2] · Ali Khansefid[3] · Aditi Kumawat[1] · Felix Schneider[1] · Johachim Wassermann[2] · Gerhard Müller[1]**

✉ Francesca Taddei
  francesca.taddei@tum.de

  Sabrina Keil
  sabrina.keil@geophysik.uni-muenchen.de

  Ali Khansefid
  khansefidali@gmail.com

  Aditi Kumawat
  aditi.kumawat@tum.de

  Felix Schneider
  felix.w.schneider@tum.de

  Johachim Wassermann
  j.wassermann@lmu.de

  Gerhard Müller
  gerhard.mueller@tum.de

[1] Chair of Structural Mechanics, Technical University of Munich (TUM), Arcisstr. 21, 80333 Munich, Germany

[2] Department of Earth and Environmental Sciences, Ludwig-Maximilians-Universität (LMU), Theresienstr. 41, 80333 Munich, Germany

[3] KPFF Inc, 1601 5th Ave, Seattle, WA 98101, USA